Applied Energy 397 (2025) 126340

Contents lists available at ScienceDirect

Applied Energy

journal homepage: www.elsevier.com/locate/apen

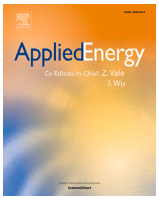

Design optimization for grid integration of a high-temperature thermal energy storage system

Ashwin Sandeep [a,b,1], Shomik Verma [a,1], Kyle Buznitsky [a], Asegun Henry [a,*]

[a] Department of Mechanical Engineering, Massachusetts Institute of Technology, Cambridge, MA 02139, USA
[b] Department of Mechanical and Process Engineering, ETH Zürich, 8092, Zürich, Switzerland

HIGHLIGHTS

- Non-linear model of thermal energy storage technology incorporated into electric power system modeling.
- Oversizing the discharge infrastructure to enable constant-power discharging can offer grid cost benefits.
- Oversizing the charging infrastructure to enable fast charging can offer grid cost benefits.
- Oversizing the storage infrastructure to enable constant-power discharging does not offer grid cost benefits.
- Systems that minimize grid costs also generally maximize investor returns.

GRAPHICAL ABSTRACT

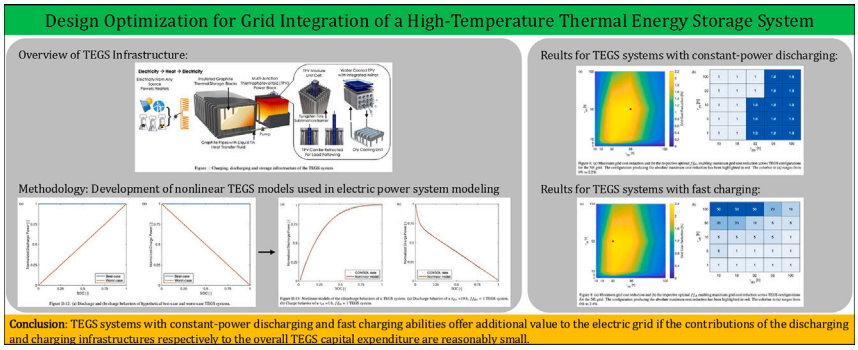

ARTICLE INFO

Keywords:
Thermal energy grid storage
Electric power system modeling
Decarbonizing electric grids

ABSTRACT

Decarbonizing the electric grid is essential for climate change mitigation and it requires a shift from fossil fuel-powered generation technologies to renewable energy technologies. The intermittency of renewables means that they can only be reliably integrated into the grid when complemented with long-duration energy storage technologies. An emerging storage technology, termed Thermal Energy Grid Storage (TEGS), has been shown to have low enough energy and power capacity costs such that it can enable a cost-effective decarbonization of the grid. The design optimization of this TEGS system for its integration into the electric grid is explored here.

TEGS systems could be designed to enable constant-power discharging and fast charging since these are critical assets for a storage technology to have. The former matches utilities' expectations of a power source while the latter enables fully utilizing cheap, excess electricity available from renewables to quickly increase the amount of energy stored in the system. Here, nonlinear models encapsulating TEGS discharge and charge behaviors are incorporated into the Capacity Expansion Model, GenX, to determine the value of constant-power discharging and fast charging of TEGS. The study shows that these improvements, enabled by oversizing the discharging/charging infrastructures can offer additional value to the grid if the discharging/ charging infrastructure costs remain relatively small compared to the overall capital expenditure.

* Corresponding author.
Email address: ase@mit.edu (A. Henry).
[1] These authors contributed equally to this work.

https://doi.org/10.1016/j.apenergy.2025.126340
Received 10 April 2025; Received in revised form 2 June 2025; Accepted 13 June 2025
Available online 25 June 2025

Acronyms

TEGS	Thermal Energy Grid Storage
VRE	Variable Renewable Energy
PHS	Pumped-Hydro Storage
CAES	Compressed Air Energy Storage
TES	Thermal Energy Storage
RTE	Round-Trip Efficiency
TPV	Thermophotovoltaic
HTF	Heat Transfer Fluid
BESS	Battery Energy Storage System
CPE	Cost per unit energy
CPP_{dis}	Cost per unit discharge power
CPP_{ch}	Cost per unit charge power
LI	Linear Interpolation
PL	Piece-wise Linear
PNL	Piece-wise Nonlinear
NE	New England
TX	Texas

1. Introduction

1.1. Context

Carbon dioxide emissions from electricity generation contribute significantly to climate change, making the transition from fossil fuel-based thermal power plants to renewable energy sources like solar and wind crucial for limiting global temperature rise. Although the adoption of variable renewable energy (VRE) resources has increased in recent years across electricity grids worldwide [1], the inherent daily, seasonal and weather-dependent intermittency associated with these technologies means that they are not dispatchable. This is where the need for energy storage arises. Energy storage technologies can charge using excess electricity from the grid during periods of high generation and low demand, store this electricity for a specific duration, and discharge during periods of low VRE generation and high demand [2]. Cost-effective decarbonization of the electric power sector requires cheap storage technologies to complement VRE resources which have become dramatically inexpensive in recent years [3]. Additionally, these technologies should exhibit the ability to adapt and respond to varying grid requirements to ensure a seamless, reliable operation of the grid.

Energy storage technologies, such as Pumped Hydro Storage (PHS) and Compressed Air Energy Storage (CAES), are limited by factors like geography and efficiency [4], while alternatives like electrochemical batteries (Li-ion, redox flow) are too expensive [2,5] for multi-day storage. These challenges highlight the need for a novel energy storage solution to enable effective decarbonization of the electric grid. Thermal energy storage (TES) has the potential to realize energy capacity costs below $20/kWh, necessary for the achievement of cost-effective multi-day storage [5,6], while also enabling a storage duration of several days, as described in [7–9]. Section 1.2 provides a general overview of TES and a detailed description of the specific incarnation of TES analyzed in this work, termed Thermal Energy Grid Storage (TEGS). This is followed by a brief review of past studies aimed at modeling the value of energy storage technologies in emerging power systems and an anticipation of the key findings in this study.

1.2. Technical overview

TES technologies offer the potential for low-cost, long-duration energy storage by storing surplus electricity from the grid as heat. The stored heat is later reconverted to electricity and discharged to the grid when demand exceeds supply. Resistance heaters and heat pumps can be used to convert electricity to heat and heat engines such as turbines [10], thermoelectrics and thermophotovoltaics [11] can be used to convert heat back to electricity. While the conversion of heat to electricity is associated with significant efficiency penalties with the Carnot efficiency imposing an upper bound on the process, storing electricity thermally rather than electrochemically tends to be vastly cheaper due to the ability to use inexpensive storage materials. Amy et al. [7] and Ziegler et al. [5] have shown that technologies which offer very low energy and power capacity costs (even if they have a low round-trip efficiency (RTE)), tend to be more profitable than batteries which are characterized by extremely high RTEs around 90 % but high capital costs. This warrants further exploration of thermal energy storage, a particular embodiment of which is TEGS.

The TEGS system is illustrated in Fig. 1. It is composed of separate charging, storage and discharging infrastructures [7] as delineated below.

Charging infrastructure: Resistance heaters are used to convert electricity from any power source on the grid into heat.

Storage infrastructure: Insulated graphite blocks are used as the storage medium for the high temperature heat.

Discharging infrastructure: Thermophotovoltaic (TPV) cells act as the heat engine to convert stored heat into electricity.

Liquid Sn is employed as the heat transfer fluid (HTF) to transfer heat via convection between the storage medium and the charging and discharging infrastructures. Both graphite and liquid Sn are characterized by high thermal conductivity and thermal stability at high temperatures and are also compatible with each other making them favorable for this application [9].

TEGS is operated at as high a temperature as possible considering material restrictions to maximize the efficiency and the power density of the TPV heat engine. A record-breaking TPV efficiency above 40 % has been recently demonstrated by LaPotin et al. [11] for a very high emitter temperature of 2400 °C. The TPV efficiency governs the RTE of the system since resistance heaters generally achieve extremely high efficiencies around 99 %. Additionally, a higher power density reduces system cost since the TPV heat engine can generate more electricity for the same area [12]. This justifies the high-temperature operation regime for TEGS. During charging, liquid Sn at 1900 °C is heated up to 2400 °C by the resistance heaters, and the Sn in turn heats up the graphite storage blocks as it flows through channels embedded in the blocks. The temperature of the graphite blocks gradually rise during charging as the amount of energy stored as sensible heat increases until it attains a maximum temperature of 2400 °C which signifies a state of charge (SOC) of 100 % and the end of the charging process. During discharging, the liquid Sn is once again heated up to 2400 °C, but this time by the graphite blocks, and the Sn in turn heats up the emitter of the TPV cells as it flows through the power block. The temperature of the graphite blocks gradually falls during discharging as more of the stored energy is released to the HTF until it attains a minimum temperature of 1900 °C which signifies an SOC of 0 % and the end of the discharging process. Several strategies exist for improving the charging and discharging operations of TES systems, as explored by Verma et al. [9] for optimizing system design for effective heat transfer. These concepts will be discussed in Section 2 from the point of view of optimizing TES system design for its integration into the electric grid.

Existing literature includes several studies that model the incorporation of energy storage technologies into electric power systems to quantify their value to the grid and evaluate the storage characteristics necessary to enable a cost-effective decarbonization [2,5,13–17]. Sepulveda et al. [13] found that the energy storage capacity cost and the discharge efficiency of long-duration storage systems are the most important performance parameters for lowering overall electricity costs,

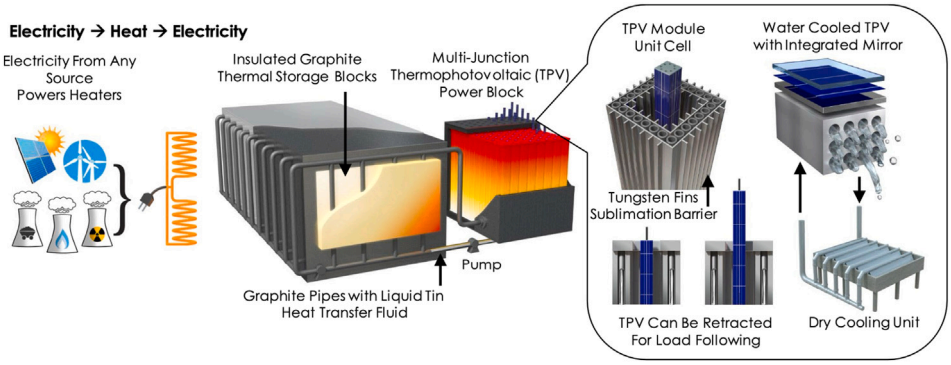

Fig. 1. Charging, storage and discharging infrastructure of the TEGS system.

with an energy capacity cost below $20/kWh being required to reduce costs by more than 10 % compared to a grid reliant on firm low-carbon generation technologies. Similarly, Ziegler et al. [5] concluded that competitive renewables-based baseload generation requires storage costs around $20/kWh in resource-abundant US regions like Texas and Arizona, and as low as $10/kWh in places like Iowa and Massachusetts. Braff et al. [2] proposed a method to evaluate storage technologies across varying energy and power cost profiles, highlighting that while current technologies like PHS and CAES can add value to solar and wind, significant reductions in both generation and storage costs are needed for profitability, with the optimal cost improvement trajectories being relatively location invariant. Li et al. [14] demonstrated through a mixed integer linear programming model that capacity co-optimization of molten salt-based TES and battery energy storage (BESS) can improve VRE utilization and reduce grid investment costs, with BESS being used for short-term, high-frequency load balancing and TES handling longer-duration storage. Meanwhile, the authors in [15] showed that coupling TES with nuclear power plants can enhance system flexibility by cycling the electrical generator to match load while allowing reactors to continue operating at constant output rather than in inefficient load-following modes, thereby achieving deep decarbonization cost-effectively by reducing VRE curtailment and avoiding the cost of additional firm generation capacity. Finally, Li et al.[16] found that integrating a generic TES system with heat pumps in urban distributed energy systems can significantly lower CO_2 emissions and overall system costs, while Amini Toosi et al. [17] reported a similar outcome in standalone residential buildings, with a payback period of approximately 15 years. So, there is abundant evidence of the benefits of TES in enabling cost-effective decarbonization in existing literature which served as a motivation for this work. However, a common theme across these studies is that they tend to focus on either existing energy storage technologies at high technology readiness levels (TRL's) or on very abstract technologies defined only by cost and performance parameters. Thus, there is a gap in evaluating the value of integrating emerging low-TRL energy storage technologies like TEGS into future power systems.

The work done by Eikeland et al. [18,19] was aimed at filling this gap in the literature by carrying out the design optimization of the TEGS system to match specific market conditions to, in turn, enable a cost-effective grid decarbonization. In [18], a TEGS unit coupled to a PV system was modeled as being part of an existing real-world grid to analyze how such a system could be valuable in combating the intermittency of VRE sources. It was found that the coupled (PV + TEGS) system increases the power availability beyond that offered by an isolated PV system thus improving the dispatchability of PV. Additionally, the power availability of such a coupled system increases with both the storage size of TEGS and the CO_2 emissions limit imposed on the grid. In [19], a stand-alone TEGS system capable of interacting with all generation resources on the grid was modeled to determine the optimal TEGS design parameters. Findings from the study indicated that a maximum operating temperature of 2400 °C and a daily heat loss of 3 % were optimal and the electric power system became approximately 4 % less expensive than the baseline scenario without TEGS for the engineering optimized TEGS unit. Additionally, this study highlighted the ability of TEGS to enable firm capacity replacement to varying degrees in order to satisfy differing grid emissions limits while also revealing how grid resiliency improves through the incorporation of TEGS. A limitation of these works however, is the use of simplified models which fail to represent the true performance characteristics of TES systems. The more realistic, physics-based models developed in this work address this issue. The results obtained from these new models were compared to those obtained from the simplified models to validate the modeling approach as a first step. Details about both the existing and newly developed TES models have been presented in Appendix D and the validation of the new modeling approach in Appendix E. The models were then used for the analysis of various TEGS performance improvement strategies including constant-power discharging, fast charging and storage oversizing, elaborated in Section 2, which form the core of this study. Thus, the analysis here aims to reveal the existence of optimal TEGS configurations different to the ones identified in [19], with the magnitude of the additional cost benefits being dependent on both the performance improvement strategy itself and the grid characteristics.

This study employs the same electricity resource Capacity Expansion Model, GenX, used in [13,18,19] to evaluate the value of TEGS in real-world grid conditions. GenX is a highly-configurable constrained optimization model with a high temporal resolution that determines the optimal mix of electricity generation, storage and transmission network investments and operational decisions to meet the electricity demand in a future planning year at lowest cost. For a more comprehensive explanation of GenX, the reader is directed to [20].

1.3. Article structure

The article comprises 4 further sections. Section 2 introduces some fundamental TEGS equations, the nominal TEGS discharge and charge behaviors which provided the motivation for exploring performance improvement strategies and the cost components of the TEGS system. This is followed by a description of the conceived TEGS performance improvement strategies along with their visualization using appropriate plots. The impact of these strategies on TEGS costs is also discussed. Section 3 provides an overview of the electric grids and TEGS configurations analyzed in this study. In Section 4, the value of the various TEGS performance improvement strategies to the grid will be determined by evaluating the impact of the TEGS system's design choices on grid performance, i.e., grid cost savings. It will be shown how some TEGS configurations are capable of offsetting increased costs at the system level to provide cost benefits at the grid level and how the design choices

that prove most cost-effective can vary based on grid characteristics and installed capacity due to the resulting variation in system-level behavior of TEGS. Finally, Section 5 consolidates the entire research with a set of conclusions along with recommendations for future work. Additionally, a case study to ascertain whether the TEGS configuration optimal for the grid would also be optimal for an investor in TEGS and thus uncover any potential conflicts of interest between the grid and the investor is presented in Appendix I.

2. Theory and calculation

2.1. Fundamental TEGS equations

The maximum energy that can be stored in the graphite storage blocks is referred to as the thermal energy capacity of TEGS and is given by

$$E = mc_{p,C}\Delta T_C, \tag{1}$$

where m is the total mass of graphite, $c_{p,C}$ is the specific heat capacity of graphite and ΔT_C is the difference between the maximum (2400 °C) and minimum (1900 °C) operating temperatures of the system and is thus equal to 500 °C.

The nominal power extracted by the HTF from the storage block during discharging is referred to as the thermal discharge power capacity of TEGS and is given by

$$P_{dis,th,nom} = \dot{m}_{dis,nom}c_{p,Sn}\Delta T_{Sn,dis,nom}, \tag{2}$$

where $\dot{m}_{dis,nom}$ is the nominal flowrate of Sn during discharging, $c_{p,Sn}$ is the specific heat capacity of Sn and $\Delta T_{Sn,dis,nom}$ is the nominal difference between the temperature of the Sn entering the storage block and that exiting the storage block. $\Delta T_{Sn,dis,nom}$ is also equal to 500 °C given the maximum and minimum operating temperatures of the system.

The electrical discharge power capacity of TEGS is defined as the nominal power output from the TPV power block to the grid. This can be related to $P_{dis,th,nom}$ through the efficiency of the power block, η_{dis}, as

$$P_{dis,el,nom} = \eta_{dis}P_{dis,th,nom}. \tag{3}$$

η_{dis} is assumed to be 50 % since further improvements over the value reported in [11] are expected in the future [21].

Thermal and electrical charge power capacities can be defined analogously to the discharge power capacities. The nominal power delivered by the HTF to the storage block during charging is referred to as the thermal charge power capacity of TEGS as is given by

$$P_{ch,th,nom} = \dot{m}_{ch,nom}c_{p,Sn}\Delta T_{Sn,ch,nom}, \tag{4}$$

where $\dot{m}_{ch,nom}$ is the nominal flowrate of Sn during charging and $\Delta T_{Sn,ch,nom}$ is the nominal difference between the temperature of the Sn entering the storage block and that exiting the storage block. This is also equal to 500 °C.

The electrical charge power capacity of TEGS is defined as the nominal power input from the grid to the resistance heater. This can be related to $P_{ch,th,nom}$ through the efficiency of the heater, η_{ch}, as

$$P_{ch,el,nom} = \frac{P_{ch,th,nom}}{\eta_{ch}}. \tag{5}$$

η_{ch} is assumed to be 99 % as mentioned previously.

The rated discharge duration of TEGS, which is defined as the time taken to fully discharge the system when operating at nominal discharge power is given by

$$\tau_{dis} = \frac{E}{P_{dis,th,nom}}. \tag{6}$$

Similarly, the rated charge duration of TEGS, which is defined as the time taken to fully charge the system when operating at nominal charge power is given by

$$\tau_{ch} = \frac{E}{P_{ch,th,nom}}. \tag{7}$$

Eqs. (6) and (7) can also be written in terms of electrical power capacities as

$$E = \frac{\tau_{dis}}{\eta_{dis}}P_{dis,el,nom} = \tau_{ch}\eta_{ch}P_{ch,el,nom}. \tag{8}$$

2.2. TEGS discharge & charge behaviors

Although TEGS systems have nominal discharge and charge powers associated with them, they are unable to always operate at these nominal powers, unlike an electrochemical battery for instance. The discharge power of TEGS drops below its nominal value during discharge because the graphite storage blocks cool as discharging progresses [9]. This causes the temperature of the Sn exiting the storage system and entering the power block to drop below the nominal operating temperature of 2400 °C resulting in a discharge power lower than the discharge power capacity of TEGS. Analogously, the charge power of TEGS also drops below its nominal value during charging. This less-than-ideal behavior of TEGS is the motivation for three of the four performance improvement strategies discussed later in this section.

Large-scale COMSOL [22] simulations of TEGS systems were performed by Verma et al. [9] to obtain an accurate depiction of the TEGS discharge and charge behaviors, the details of which have been summarized in Appendix A. These behaviors are visualized in Fig. 2 for a variety of TEGS systems through plots showing the variation of normalized (dis)charge powers with the SOC of the system, where SOC is defined as the ratio of the instantaneous energy stored to the energy capacity of the system. TEGS systems can be fully characterized by their τ_{dis} and τ_{ch} because the behavior of a TEGS system is equivalent to that of multiple smaller systems operating in parallel. For instance, the operation of a 10 GWh system with (dis)charge powers of 1 GW and 2 GW respectively is equivalent to that of ten parallel 1 GWh systems with (dis)charge powers of 0.1 GW and 0.2 GW.

2.3. Cost components of TEGS

The capital expenditure (CAPEX) associated with TEGS can be divided into: (a) Cost per unit energy (CPE), (b) Cost per unit discharge power (CPP_{dis}) and (c) Cost per unit charge power (CPP_{ch}). CPE will be expressed in units of $/kWh-th and the CPP's in units of $/kW-e. The three cost components have been described below.

CPE: CPE embodies the cost of the storage infrastructure. It is mathematically represented as

$$CPE = \frac{Total\ cost\ of\ storage\ infrastructure}{E}, \tag{9}$$

where the biggest contributors to storage infrastructure costs are the Sn HTF, graphite storage medium, insulation layers for the storage blocks and construction costs [8].

It was shown in [8] that CPE decreases with increasing system size due to reduced insulation requirements and ultimately drops to below the $20/kWh-e target for system sizes around 1 GWh. Thus, it is assumed in this study that modular TEGS units of 1 GWh capacity (and maximum operating temperature of 2400 °C and daily heat loss of 3 % deemed optimal in [19]) will be implemented in the grid. The CPE for such a system would be approximately $9/kWh-th.

CPP_{dis}: CPP_{dis} captures the costs associated with the discharging infrastructure. It is mathematically represented as

$$CPP_{dis} = \frac{Total\ cost\ of\ discharging\ infrastructure}{P_{dis,el}}, \tag{10}$$

where the biggest contributors to discharging infrastructure costs are the TPV cells, cooling system for the TPV cells and inverter [8].

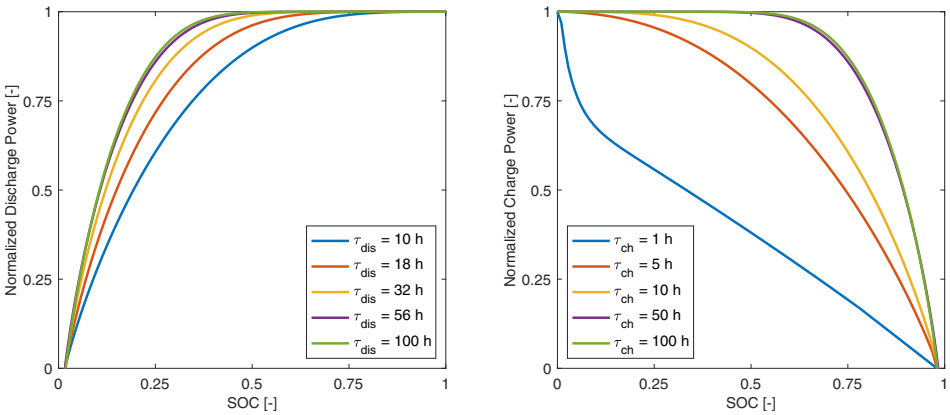

Fig. 2. Variation of (dis)charge powers with SOC for a range of TEGS rated (dis)charge durations.

It was shown in [8] that CPP_{dis} increases marginally with the power capacity of the system. For instance, the CPP_{dis} of a 10 MW system would be ¢56.2/W-e while that of a 100 MW system would be ¢56.7/W-e.

***CPP*$_{ch}$**: CPP_{ch} captures the costs associated with the charging infrastructure. It is mathematically represented as

$$CPP_{ch} = \frac{Total\ cost\ of\ charging\ infrastructure}{P_{ch,el}}, \tag{11}$$

where the biggest contributors to charging infrastructure costs are the heater controller and the graphite pipes and headers for transporting Sn. CPP_{ch} is fully independent of the power capacity of the system and has a constant value of ¢1.7/W-e.

The detailed calculation of these three cost components of TEGS has been presented in Appendix B.

2.4. Constant-power discharging

As explained in Section 2.2, it is difficult for a TEGS system to provide constant, nominal power throughout discharge. This is a cause for concern because utilities would expect a constant power from storage resources, as offered by most established storage technologies. Thus, when integrating TEGS into the grid, it is essential to be able to maintain the discharge power constant at its nominal value and this requirement is the motivation for the first performance improvement strategy devised.

Based on the equations presented in Section 2.1, the actual discharge power of TEGS (discharge power refers to thermal discharge power from here on unless otherwise mentioned) is given by

$$P_{dis,th,act}(t) = \dot{m}_{dis,nom} c_{p,Sn} \Delta T_{Sn,dis}(t), \tag{12}$$

where $\Delta T_{Sn,dis}(t)$ is the instantaneous difference between the Sn temperatures at the storage inlet (which is always assumed to be 1900 °C) and outlet and is $\leq \Delta T_{Sn,dis,nom}$.

In order to maintain the TEGS discharge power constant at its nominal value, the instantaneous flowrate of Sn during discharging, $\dot{m}_{dis}(t)$, can be ramped up above its nominal value to match the drop in $\Delta T_{Sn,dis}(t)$ [9] such that

$$\frac{\dot{m}_{dis}(t)}{\dot{m}_{dis,nom}} = \frac{\Delta T_{Sn,dis,nom}}{\Delta T_{Sn,dis}(t)}. \tag{13}$$

The maximum value to which the flowrate can be raised, $\dot{m}_{dis,\max}$, determines the minimum Sn temperature at the storage outlet, $\Delta T_{Sn,dis,\min}$, that can still ensure nominal discharge power, and the ratio of this maximum flowrate to the nominal flowrate is termed the discharge flowrate factor, ff_{dis}. Thus,

$$ff_{dis} = \frac{\dot{m}_{dis,\max}}{\dot{m}_{dis,nom}} = \frac{\Delta T_{Sn,dis,nom}}{\Delta T_{Sn,dis,\min}}. \tag{14}$$

When $\Delta T_{Sn,dis}(t)$ eventually drops below $\Delta T_{Sn,dis,\min}$, nominal discharge power can no longer be achieved since $\dot{m}_{dis}(t)$ cannot be increased any further. As an example, an ff_{dis} of 5 implies that nominal discharge power will be available even when the Sn outlet temperature drops to 2000 °C from the nominal 2400 °C. However, if Sn temperature decreases further, output power will drop below the nominal value.

For TEGS systems equipped with this ability to dynamically alter the Sn flowrate according to the Sn temperature at the storage outlet, the extreme mode of operation characterized by $\dot{m}_{dis,\max}$ and $\Delta T_{Sn,dis,\min}$, determines the sizing of the infrastructure and thus, the CAPEX of the system. The infrastructure changes and cost implications of implementing this performance improvement strategy are two-fold. First, a larger pump capable of delivering the maximum flowrate, $\dot{m}_{dis,\max}$, will be required. Pumping costs scale linearly with flowrate and hence with ff_{dis}. However, since pumping costs are minute in comparison to the other contributions to CPP_{dis}, the increase in CPP_{dis} due to the use of a larger pump will also be marginal. Second, and more importantly, a larger TPV array will be required. Since the power density of TPV cells is proportional to the emitter temperature [11], the amount of electricity a given surface area of TPV cells can generate will reduce as the temperature of Sn entering the power block decreases. This in turn means that the TPV cells would need to be over-built, with more cells being exposed to the emitter as the Sn temperature decreases, to generate nominal electrical discharge power when lower-grade heat is input to the TPV power block [9]. This has much more significant cost implications than the increased pumping requirements since the TPV cost is the biggest contributor to CPP_{dis}.

The variation of CPP_{dis} with ff_{dis} for a 100 MW system is illustrated in Fig. 3(a) which elucidates the increase in TPV requirements with increasing ff_{dis}. The increase in CPP_{dis} with ff_{dis} levels off at high values of ff_{dis} because the TPV power density varies nonlinearly (i.e., T^4) with emitter temperature, with its decrease being limited at lower temperatures.

The effect of this performance improvement strategy is visualized in Fig. 3(b) which shows the variation of discharge power with SOC for a TEGS system with τ_{dis} = 10 h. As can be observed, increasing ff_{dis} to above 1 dramatically changes the discharge behavior of TEGS, with the system being able to output nominal discharge power even at an SOC as low as 10 % when an ff_{dis} of 10 is used. The variation of Sn outlet temperature with SOC for the same system is illustrated in Fig. C.12(a).

The trade-off analysis performed using GenX, the results of which are presented in Section 4.1, was aimed at yielding the ideal ff_{dis} for which the improvement in TEGS discharge performance, illustrated in Fig. 3(b),

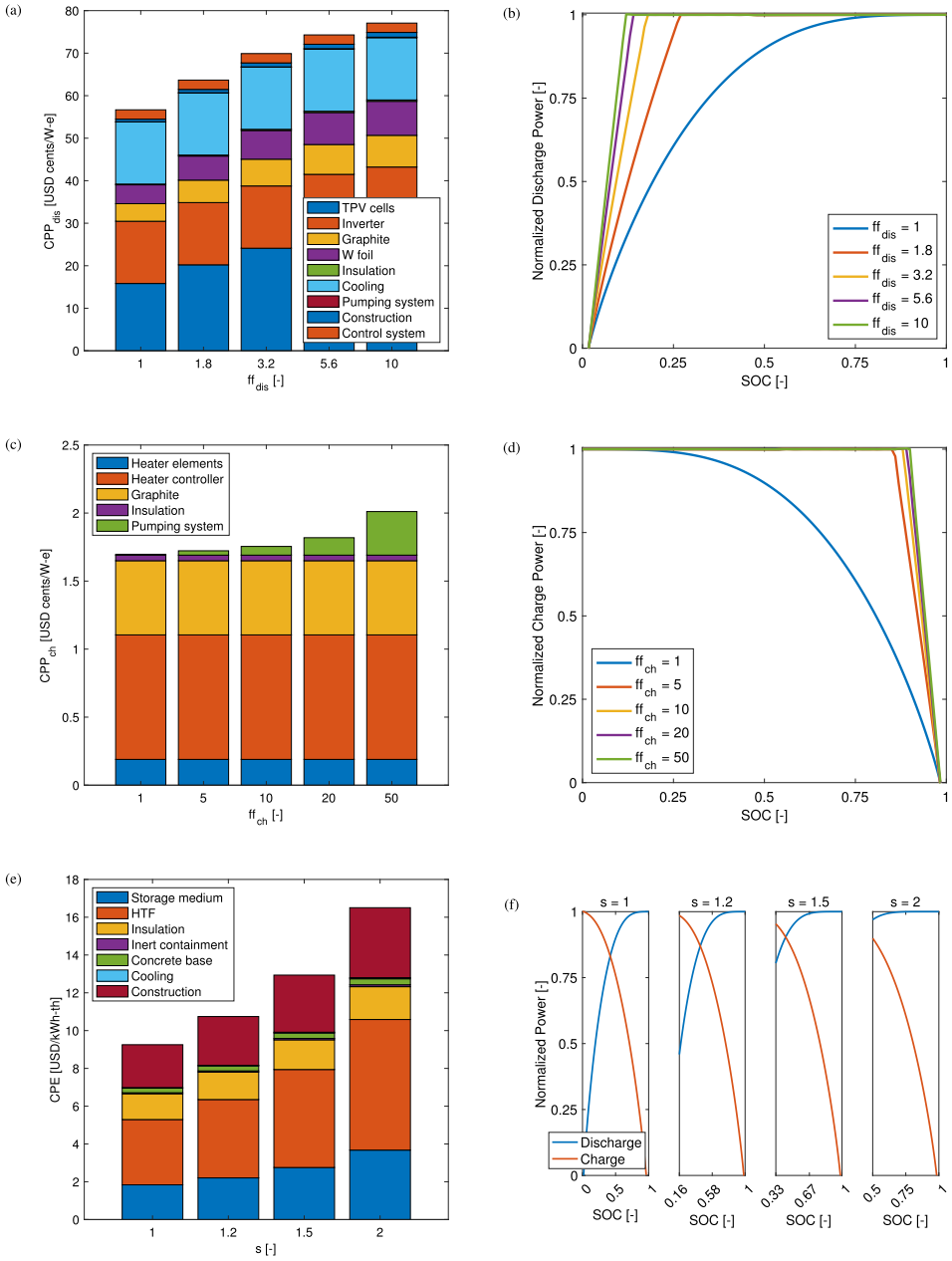

Fig. 3. Effects of the various TEGS performance improvement strategies on costs and operation. (a) Variation of CPP_{dis} with ff_{dis} for a 100 MW TEGS system. Note the increase in CPP_{dis} with ff_{dis} leveling off at high ff_{dis} values. (b) Variation of discharge power with SOC for a TEGS system with $\tau_{dis} = 10$ h for increasing ff_{dis} values. (c) Variation of CPP_{ch} with ff_{ch} (for all TEGS systems independent of power capacity). (d) Variation of charge power with SOC for a TEGS system with $\tau_{ch} = 10$ h for increasing ff_{ch} values. (e) Variation of CPE with s for a TEGS system with 1 GWh E_{eff}. (f) Variation of discharge and charge powers with SOC for a TEGS system with $\tau_{dis} = 10$ h and $\tau_{ch} = 5$ h for increasing s values.

outweighs the increase in discharge infrastructure CAPEX, illustrated in Fig. 3(a), for different scenarios.

2.5. Constant-power charging

Periods when excess electricity is available from VRE sources are utilized by energy storage technologies to charge and increase their SOC. However, fluctuating electricity prices and potential competition among various energy storage resources mean that the ability to charge quickly is valuable to minimize the cost of charging. This requirement is the motivation for the second performance improvement strategy devised.

Maintaining a constant charge power for longer enables faster charging by definition. The implementation of this performance improvement strategy is analogous to that of constant-power discharging. Thus, equations analogous to Equations [12-14] developed in Section 2.4 can be used to model constant-power charging and are not re-explained for brevity.

An added advantage of this strategy is that the only infrastructure change that would be required is the installation of a larger pump to enable $\dot{m}_{ch,\max}$, the maximum value to which the flowrate can be raised. No changes to the heater are necessary since the maximum charging power never exceeds its nominal value. Furthermore, the CPP_{ch} varies little with the charge flowrate factor, ff_{ch}, as illustrated in Fig. 3(c), due to the marginal contribution of pumping costs to the total infrastructure cost. This means that higher flowrates than that considered for constant-power discharging can be explored.

As previously, the effect of this performance improvement strategy is visualized in Fig. 3(d) which shows the variation of charge power with SOC for a TEGS system with $\tau_{ch} = 10$ h. As can be observed, the change in the charge behavior of TEGS when ff_{ch} is increased beyond 1, with the system being able to charge at nominal power even at an SOC as high as 90 % for an ff_{ch} of 10, is similar to the change in its discharge behavior when ff_{dis} is raised above 1 since the system dynamics remain identical but in reversed directions. The variation of Sn outlet temperature with SOC for the same system is illustrated in Fig. C.12(b).

As with constant-power discharging, the trade-off analysis performed using GenX, the results of which are presented in Section 4.2, was aimed at yielding the ideal ff_{ch} for which the improvement in TEGS charge performance, illustrated in Fig. 3(d), outweighs the increase in charge infrastructure CAPEX, illustrated in Fig. 3(c), for different scenarios.

2.6. Oversized energy storage

The objective of this performance improvement strategy is to once again achieve constant discharge power. However, unlike in Section 2.4, changes are made to the storage infrastructure rather than the discharging infrastructure to achieve this objective.

This strategy involves replacing the nominal 1 GWh modules which cycle between SOCs of 1 and 0 with oversized units (i.e., units with a higher energy capacity) with a non-zero lower bound on SOC. While the energy capacity of the oversized units will be greater than 1 GWh, their effective energy capacity, E_{eff}, which can be defined as the maximum *usable* energy stored in the graphite blocks will still be 1 GWh due to the constraint on minimum SOC. The motivation for doing this is that the TEGS system would no longer have to operate in low-SOC regions where its discharge power drops well below its nominal value, thus enabling relatively constant discharge power throughout its operation regime. However, this comes with two caveats. First, additional costs associated with building up excess unused capacity will need to be borne and second, operating in the high-SOC region means that the maximum charging power will always be less than nominal due to the graphite blocks never cooling down to 1900 °C.

An oversizing factor given by

$$s = \frac{E}{E_{eff}}, \tag{15}$$

where $s > 1$, determines how much greater the energy capacity of the oversized system is than 1 GWh on a fractional basis. The minimum value that the SOC of such a system can drop to will be $SOC_{\min} = 1 - \frac{1}{s}$.

As an example, $s = 1.5$ represents a module with an energy capacity of 1.5 GWh. $SOC_{\min}$ of such a system would be 0.33 implying that only 67 % of the total energy capacity (i.e., 1 GWh) is available to be used.

The storage infrastructure cost corresponds to the energy capacity of the system. While it was shown in [8] that CPE decreases with increasing system size due to reduced insulation requirements, the CPE of the oversized systems would be higher than that of the nominal system since CPE in this context is the storage infrastructure cost per E_{eff} rather than E to capture the cost of the actual energy available. The variation of CPE with s for a TEGS system with an E_{eff} of 1 GWh is illustrated in Fig. 3(e).

The effect of this performance improvement strategy is visualized in Fig. 3(f) through plots showing the variation of both the discharge and charge powers with SOC for a TEGS system with $\tau_{dis} = 10$ h and $\tau_{ch} = 5$ h oversized to different levels. As can be observed, increasing $SOC_{\min}$ with increasing s forces the discharge power to always be near-constant at their nominal values for high s values.

As with the other improvement strategies, the trade-off analysis performed using GenX should yield the ideal s for which the improvement in TEGS discharge performance, illustrated in Fig. 3(f), outweighs the increase in storage infrastructure CAPEX, illustrated in Fig. 3(e), for different scenarios.

3. Materials and methods

3.1. Electric grid modeling in GenX

Two grids are analyzed here. The first one covers the state of Massachusetts in the New England (NE) region of the US and is operated by the Independent System Operator-New England (ISO-NE). The second one covers the state of Texas (TX) in the southern US and is operated by the Electric Reliability Council of Texas (ERCOT). Modeling two different grid regions enables the comparison of the value of energy storage technologies in different settings characterized by unique climates and load patterns. Climatic conditions influence the capacity factors of VRE resources and electricity demand patterns leading to different optimal resource mixes and energy storage requirements for different grid regions. The NE region has a large potential for wind power due to its high latitude while TX receives abundant solar power. The analysis in [19] showed that while the value of TEGS is comparable across both grids, there are variations in the optimal TEGS configurations (relevant results have been discussed in Appendix E). For instance, the optimal TEGS (dis)charge durations for the NE grid were significantly higher than those for the TX grid which is a direct consequence of the high periodicity of solar power availability in TX compared to the less periodic wind power availability in NE. Additionally, while the optimal discharge and charge durations were comparable for the NE grid, the optimal charge duration was approximately half the optimal discharge duration for the TX grid in order to satisfy the requirement to charge rapidly during mid-day when abundant sunshine is available. The optimal TEGS capacities installed were also disparate across the two grids, with that in TX being an order of magnitude higher than that in NE, due to the much higher load on the TX grid which covers a much larger geographic area. Thus, grid-specific factors like the VRE mix and demand patterns can influence optimal design choices which is why both grids are analyzed in this study as well. Details regarding the collection and processing of cost and performance data of different technologies, electricity demand data and climatic data for the two grid regions studied are provided in [19].

In GenX, the electric grids were simulated for a single year at hourly resolution and a single-node representation of grids was used, i.e., the modeling and optimization of transmission and distribution networks across grid zones were avoided to manage simulation complexity. Additionally, the grids were primarily modeled as “greenfield” systems, i.e., the grids were assumed to have no existing generation or storage resources with optimal capacities of the various available technologies being built from scratch. A constraint on the maximum allowed CO_2 emissions was the sole policy constraint modeled. Only the 99 % emissions reduction scenario was modeled here due to the interest in simulating a fully decarbonized grid.

3.2. TEGS configurations analyzed

The TEGS configurations studied across the analyses presented in Section 4 are described here. The τ_{dis} values considered were 10 h, 18 h, 32 h, 56 h and 100 h (logarithmic spacing between 10 and 100) while the τ_{ch} values considered were 1 h, 5 h, 10 h, 50 h and 100 h. This resulted in 25 unique TEGS configurations since TEGS systems are characterized by the (τ_{dis}, τ_{ch}) pair. τ_{ch} values smaller than τ_{dis} values have been explored due to the observation in [19] that optimal systems tend to have a smaller charge duration than discharge duration. The CPE and CPP_{ch} remain identical across these 25 configurations, given the explanations in Section 2.3, while the CPP_{dis} decreases slightly with increasing τ_{dis} of the TEGS modules.

Section 4.1 presents the analysis of TEGS systems equipped with constant-power discharging. Such a TEGS system requires the definition of its ff_{dis}, in addition to its rated durations, for its characterization since the discharge behavior varies with both τ_{dis} and ff_{dis}, as explained in Section 2.4. Logarithmic spacing between 1 and 10 was used to derive

the ff_{dis} values considered in this analysis and is given by

$$\mathbf{ff_{dis}} = \begin{bmatrix} 1 & 1.8 & 3.2 & 5.6 & 10 \end{bmatrix}. \quad (16)$$

Each of the 25 TEGS configurations was thus analyzed at five different ff_{dis} values.

Analogously, Section 4.2 presents the analysis of TEGS systems equipped with constant-power charging. Such a TEGS system requires the definition of its ff_{ch}, in addition to its rated durations, for its characterization since the charge behavior varies with both τ_{ch} and ff_{ch}. The ff_{ch} values considered in this analysis are given by

$$\mathbf{ff_{ch}} = \begin{bmatrix} 1 & 5 & 10 & 20 & 50 \end{bmatrix}. \quad (17)$$

Higher values of ff_{ch} than those of ff_{dis} are considered because the increase in CPP_{ch} with ff_{ch} is much more marginal than the increase in CPP_{dis} with ff_{dis} meaning very high ff_{ch} values could very well be optimal.

As before, each TEGS configuration was analyzed at the five different ff_{ch} values.

Section 4.3 presents the analysis of TEGS systems equipped with oversized energy storage. Such a TEGS system requires the definition of its s, in addition to its rated durations, for its characterization since the discharge behavior varies with both τ_{dis} and s. The s values considered in this analysis are given by

$$\mathbf{s} = \begin{bmatrix} 1 & 1.2 & 1.5 & 2 \end{bmatrix}. \quad (18)$$

Each of the 25 TEGS configurations was thus analyzed at four different s values.

4. Results and discussion

Since the overall objective of GenX is to produce a *minimal-cost grid* by installing and operating the available resources optimally such that the electricity demand in a particular grid region over the modeled year is satisfied while also respecting the CO_2 emissions limit, all results are presented in terms of the grid cost savings compared to a baseline scenario without TEGS. Additionally, only the results for the NE grid are presented in the main body with the results for the TX grid presented in the appendix for brevity.

4.1. Analysis of TEGS with constant-power discharging

The aim of this analysis was to determine the value of constant-power discharging to the grid and identify the optimal TEGS configuration when constant-power discharging is incorporated into the design. Two types of analyses were performed. In the first analysis, optimal TEGS capacities were allowed to be installed on the grid while in the second analysis, the TEGS capacities installed were explicitly fixed and not left as GenX decision variables. The second analysis, done to understand the impact of under/overbuilding TEGS capacity on overall grid cost and operation, was performed by fixing the TEGS installed capacities at values lower and higher than the optimal capacities found to be installed in the first analysis. In both analyses, the 125 unique TEGS systems, represented by $(\tau_{dis}, \tau_{ch}, ff_{dis})$ triplets, obtained by sweeping the 25 (τ_{dis}, τ_{ch}) pairs over the 5 discharge flowrate factors, as discussed in Section 3.2, were simulated to determine the grid cost reduction achieved by each configuration and subsequently identify the flowrate factor which maximized the cost reduction for each (τ_{dis}, τ_{ch}) pair. The results that follow are thus presented in terms of this maximum grid cost reduction and the flowrate factor enabling the maximum cost reduction for each (τ_{dis}, τ_{ch}) pair.

4.1.1. Optimal TEGS capacity

Fig. 4 shows the maximum cost reduction achieved for the NE grid across the (τ_{dis}, τ_{ch}) pairs analyzed and the optimal flowrate factor which produced the maximum grid cost reduction for each pair. Additionally, Fig. F.16 in Appendix F.1 illustrates the respective installed energy capacities. Fig. G.18 in Appendix G.1 presents analogous results for the TX grid.

Fig. 4 illustrates that for the NE grid, no improvement to discharge uniformity, i.e., $ff_{dis} = 1$, is optimal for TEGS systems with small rated discharge durations while a small improvement in discharge uniformity, i.e., $ff_{dis} = 1.8$, is optimal for TEGS systems with large rated discharge durations. Since a similar trend is observed for the TX grid, as illustrated in Fig. G.18, the optimality of a flowrate factor seems to be more dependent on the TEGS configuration than the grid characteristics, and the improvement in discharge uniformity offered by $ff_{dis} > 1$ appears to outweigh the associated increase in cost only for TEGS systems with a large τ_{dis}, especially for large τ_{ch} values.

Differences in the percentage increase in cost associated with rising flowrates explain why a higher flowrate factor is optimal for certain TEGS configurations. Increasing ff_{dis} to a value above 1 results in a certain percentage increase in $CAPEX_{dis}$ [USD/kWh-th] which is nearly independent of TEGS configuration. However, since the contribution of the discharging infrastructure to the total CAPEX varies with system configuration, this particular percentage increase in $CAPEX_{dis}$ results in varying percentage increases in $CAPEX_{tot}$ across TEGS configurations. This effect is illustrated in Fig. 5 where it can be observed that the contribution of $CAPEX_{dis}$ to $CAPEX_{tot}$ decreases with increasing rated discharge duration and as a direct consequence, the percentage rise in total CAPEX for a given increase in flowrate factor, i.e., for a similar rise in $CAPEX_{dis}$, is lower for systems with large rated discharge durations. As an example, increasing ff_{dis} from 1 to 10 for both a

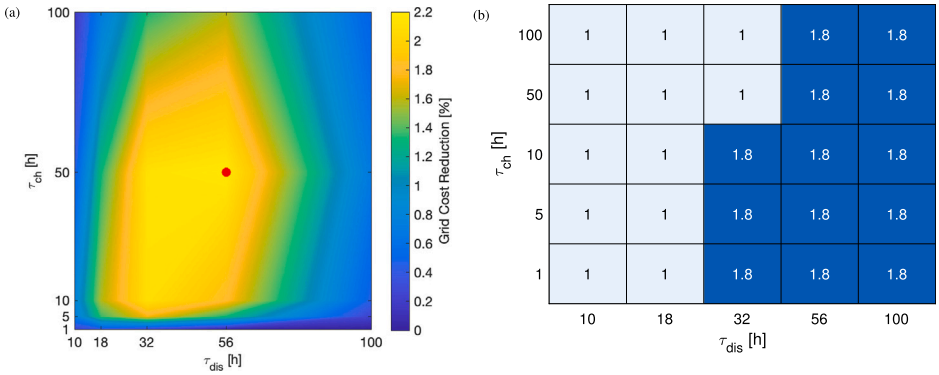

Fig. 4. (a) Maximum grid cost reduction and (b) the respective optimal ff_{dis} enabling maximum grid cost reduction across TEGS configurations for the NE grid. The colorbar in (a) ranges from 0 % to 2.2 %. The (τ_{dis} = 56 h, τ_{ch} = 50 h, ff_{dis} = 1.8) system produces the maximum cost reduction of 2.2 % and has been highlighted in red.

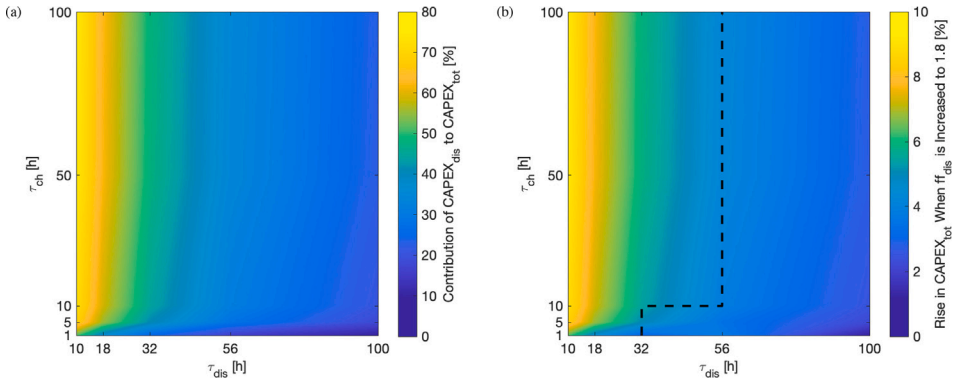

Fig. 5. (a) Contribution of $CAPEX_{dis}$ to $CAPEX_{tot}$ and (b) the rise in $CAPEX_{tot}$ when ff_{dis} is increased from 1 to 1.8 across TEGS configurations. The colorbar in (a) ranges from 0 % to 80 % and that in (b) from 0 % to 10 %. The dotted line in (b) splits the plot into two halves wherein for configurations to the left of the line, $ff_{dis} = 1$ is optimal because the rise in $CAPEX_{tot}$ when ff_{dis} is increased to 1.8 exceeds the threshold for $ff_{dis} = 1.8$ to be optimal.

($\tau_{dis} = 100$ h, $\tau_{ch} = 1$ h) system and a ($\tau_{dis} = 10$ h, $\tau_{ch} = 1$ h) system results in an increase of about 36 % in $CAPEX_{dis}$. However, this translates to an increase in $CAPEX_{tot}$ of only 3 % for the former while an increase of 19 % for the latter because the contribution of the discharging infrastructure to the total CAPEX is much lower for the ($\tau_{dis} = 100$ h, $\tau_{ch} = 1$ h) system compared to the ($\tau_{dis} = 10$ h, $\tau_{ch} = 1$ h) system.

Additionally, there appears to be a threshold for this percentage increase in total CAPEX with increasing flowrate factor beyond which the improvement in performance offered by the higher maximum flowrate does not make up for the associated increase in cost. Based on the simulations performed, the value of this threshold seems to be approximately 5 % with a minor dependence on system configuration and grid characteristics (due to variations in how different TEGS systems are utilized by different grids). This threshold is exceeded when the flowrate factor increases to 1.8 for systems which show an optimum at $ff_{dis} = 1$ while for systems which show an optimum at $ff_{dis} = 1.8$, it is exceeded only when the flowrate factor increases to even higher values. If a finer range of flowrate factors is analyzed, the threshold could be identified with greater accuracy, and systems which currently show an optimum at $ff_{dis} = 1$ will likely show an optimum at an ff_{dis} between 1 and 1.8 such that the percentage increase in total CAPEX does not exceed the threshold. Moreover, the value of this optimal flowrate factor will increase with decreasing contribution of the discharging infrastructure to total CAPEX. This hypothesis is verified in the charging analysis where such a situation arises.

It is also observed that with constant-power discharging incorporated into TEGS design, the global optimum for the NE grid shifts from installing a ($\tau_{dis} = 32$ h, $\tau_{ch} = 50$ h) system which produced a cost reduction of 2.1 % to installing a ($\tau_{dis} = 56$ h, $\tau_{ch} = 50$ h, $ff_{dis} = 1.8$) system generating a cost reduction of 2.2 %. For the TX grid, installing a ($\tau_{dis} = 18$ h, $\tau_{ch} = 10$ h) system which produces a cost reduction of 1.3 % remains optimal, indicating the benefit of constant-power discharging depends on the grid characteristics (the optimal TEGS configurations when no performance improvement strategies are incorporated into TEGS design are discussed in Appendix E).

The fact that constant-power discharging offers additional value for the NE grid but not for the TX grid can be attributed to the fundamental differences in VRE resource availability across the two grids. In the utility PV dominated TX grid, periodic variations in solar power availability mean that a system capable of discharging quickly during sunset hours is more valuable than one offering constant discharge power for long durations across days which explains why the ($\tau_{dis} = 18$ h, $\tau_{ch} = 10$ h) system remains the global optimum. However, the less periodic variations in wind availability in the onshore wind dominated NE grid mean that the ability of storage systems to provide constant power over long durations to cover windless days becomes valuable explaining why the global optimum shifts from the ($\tau_{dis} = 32$ h, $\tau_{ch} = 50$ h) system to the ($\tau_{dis} = 56$ h, $\tau_{ch} = 50$ h, $ff_{dis} = 1.8$) system.

Finally, the metric of optimality could be changed from absolute grid cost reduction to marginal grid cost reduction, i.e., grid cost saved per investment cost of TEGS [USD/USD], to address the often limited financial resources available for implementing clean energy technologies on the grid. Such an analysis to identify the optimal TEGS configuration in terms of marginal grid cost reduction has been presented in Appendix H.1.

4.1.2. Under/ overbuilt TEGS capacity

Fig. 6 shows the maximum cost reduction achieved for the NE grid across the (τ_{dis}, τ_{ch}) pairs analyzed and the optimal flowrate factor which produced the maximum grid cost reduction for each pair when the TEGS capacity was underbuilt (20 GWh) and overbuilt (400 GWh) compared to the optimal capacities installed in the previous analysis (minimum and maximum values of approximately 30 GWh and 330 GWh, as illustrated in Fig. F.16 in Appendix F.1). Fig. G.19 in Appendix G.1 presents analogous results for the TX grid where the installed TEGS capacities were 100 GWh and 500 GWh (minimum and maximum optimal capacities were around 150 GWh and 450 GWh, as illustrated in Fig. G.18(c) in Appendix G.1).).

As can be observed from Fig. 6, for the NE grid, when TEGS capacity is underbuilt, a small improvement in discharge uniformity, i.e., $ff_{dis} = 1.8$, becomes optimal for some systems for which no improvement to discharge uniformity, i.e., $ff_{dis} = 1$, was optimal previously and vice-versa when TEGS capacity is overbuilt. A similar trend is observed for the TX grid, as illustrated in Fig. G.19. When TEGS capacity is underbuilt, a higher percentage increase in $CAPEX_{tot}$ with ff_{dis} can be withstood for the associated improvement in performance. This is because underbuilding causes storage systems to cycle more. Thus, there is greater value in maintaining nominal discharge power in the low-SOC range due to more instances of low-SOC operation. Analogously, when TEGS capacity is overbuilt, a lower percentage increase in $CAPEX_{tot}$ with ff_{dis} is withstood for the associated improvement in performance. This is because overbuilding means storage systems would need to cycle less. Thus, there is less value in maintaining nominal discharge power in the low-SOC range due to less instances of low-SOC operation. This variation in operation with variation in installed capacity is evidenced in Fig. 7 which shows the SOC profiles of all the TEGS configurations analyzed over the simulated year for the NE grid. Fig. G.20 in Appendix G.1 presents analogous results for the TX grid.

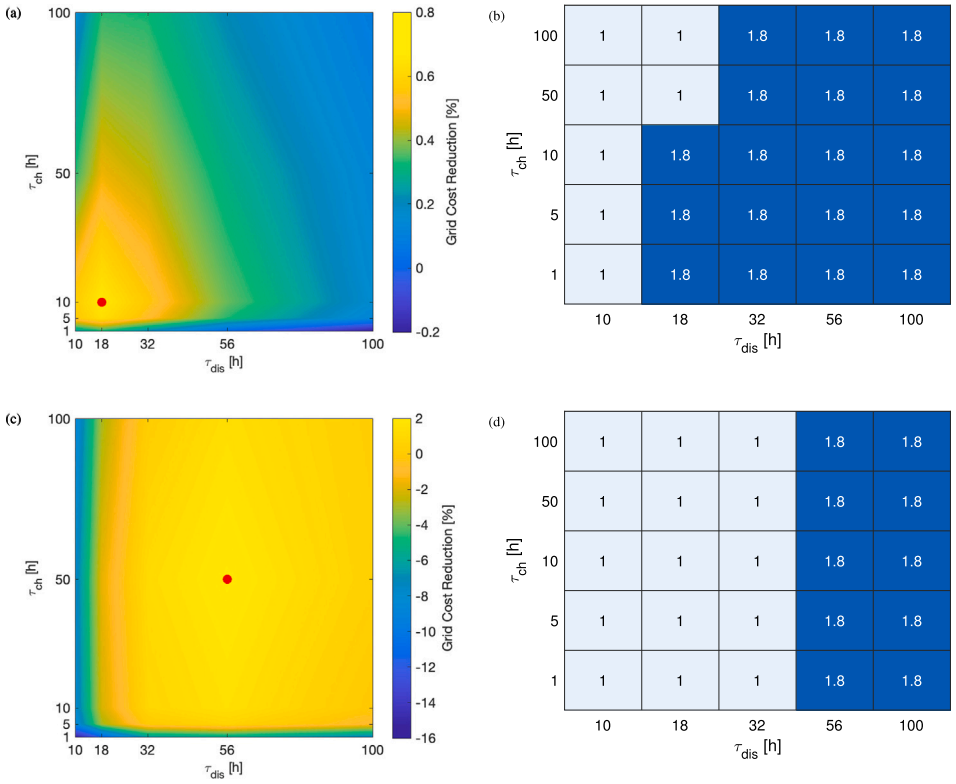

Fig. 6. (a) Maximum grid cost reduction and (b) the respective optimal ff_{dis} enabling maximum grid cost reduction across TEGS configurations for the NE grid when TEGS installed capacity is fixed at 20 GWh. (c) Maximum grid cost reduction and (d) the respective optimal ff_{dis} enabling maximum grid cost reduction across TEGS configurations for the NE grid when TEGS installed capacity is fixed at 400 GWh. The colorbar in (a) ranges from -0.2 % to 0.8 % and that in (c) from -16 % to 2 %. The ($\tau_{dis} = 18$ h, $\tau_{ch} = 10$ h, $ff_{dis} = 1.8$) and ($\tau_{dis} = 56$ h, $\tau_{ch} = 50$ h, $ff_{dis} = 1.8$) systems produce the maximum cost reductions of 0.7 % and 2.0 % when capacity is underbuilt and overbuilt respectively and have been highlighted in red. Note the shorter duration systems producing greater cost reductions when capacity is underbuilt and the longer duration systems producing greater cost reductions when capacity is overbuilt.

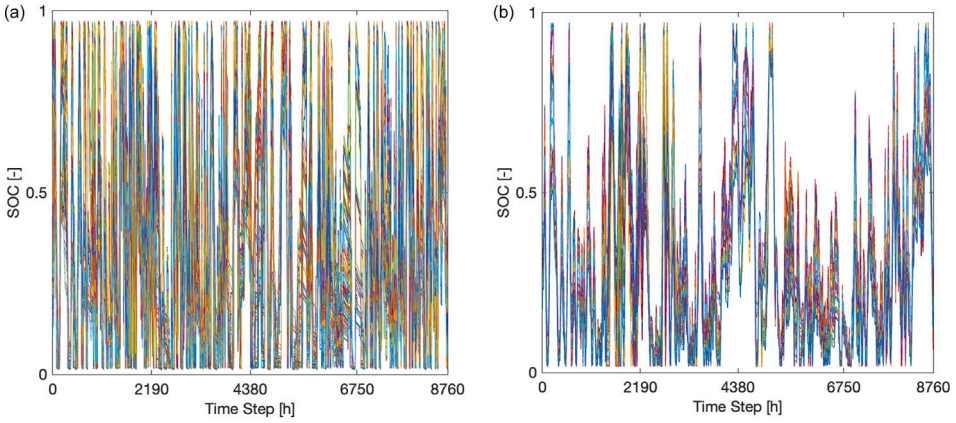

Fig. 7. SOC profiles of TEGS configurations over the studied year for the NE grid when TEGS capacity is (a) underbuilt (20 GWh) and (b) overbuilt (400 GWh). Note the much higher frequency of SOC cycling between 0 and 1 when capacity is underbuilt.

Additionally, Figs. 6 and G.19 illustrate that underbuilding causes shorter duration systems to produce greater cost reductions while overbuilding results in longer duration systems producing greater cost reductions. This can be explained in terms of the changing system-level behavior of TEGS with capacity and configuration. Arbitrage opportunities become more prevalent when there is less storage capacity on the grid. Also, storage systems with the ability to (dis)charge quickly are more suited for arbitrage since they can fully utilize rapid price fluctuations. This is why shorter duration systems produce greater cost reductions than longer duration ones when capacity is underbuilt. When there is plentiful storage capacity on the grid, the value addition of TEGS is more through grid balancing and firm capacity replacement. It is more cost-effective to use longer duration systems for extended (dis)charging rather than derating shorter duration systems to fulfill this role which is precisely why longer duration systems achieve greater cost reductions when capacity is overbuilt.

Table 1 summarizes the main findings from the analysis of TEGS with constant-power discharging.

Table 1
Summary of key performance outcomes and associated TEGS configurations.

Performance outcome	TEGS configuration	Grid cost reduction
Maximum grid cost reduction for the NE grid when optimal capacity is built	(τ_{dis} = 56 h, τ_{ch} = 50 h, ff_{dis} = 1.8)	2.2 %
Maximum grid cost reduction for the NE grid when capacity is underbuilt	(τ_{dis} = 18 h, τ_{ch} = 10 h, ff_{dis} = 1.8)	0.7 %
Maximum grid cost reduction for the NE grid when capacity is overbuilt	(τ_{dis} = 56 h, τ_{ch} = 50 h, ff_{dis} = 1.8)	2.0 %
Maximum grid cost reduction for the TX grid when optimal capacity is built	(τ_{dis} = 18 h, τ_{ch} = 10 h, ff_{dis} = 1)	1.3 %
Maximum grid cost reduction for the TX grid when capacity is underbuilt	(τ_{dis} = 18 h, τ_{ch} = 5 h, ff_{dis} = 1.8)	0.8 %
Maximum grid cost reduction for the TX grid when capacity is overbuilt	(τ_{dis} = 18 h, τ_{ch} = 10 h, ff_{dis} = 1)	1.3 %
Maximum marginal grid cost reduction for the NE grid	(τ_{dis} = 32 h, τ_{ch} = 50 h, ff_{dis} = 1.8)	0.55 [USD/USD]
Maximum marginal grid cost reduction for the TX grid	(τ_{dis} = 32 h, τ_{ch} = 10 h, ff_{dis} = 1)	0.74 [USD/USD]

4.2. Analysis of TEGS with constant-power charging

The aim of this analysis was to determine the value of constant-power charging to the grid and identify the optimal TEGS configuration when constant-power charging is incorporated into the design. As before, analyses where optimal TEGS capacities are allowed to be installed and TEGS capacities are under/overbuilt are both undertaken. Analogous to constant-power discharging, the 125 unique TEGS systems, represented by (τ_{dis}, τ_{ch}, ff_{ch}) triplets, obtained by sweeping the 25 (τ_{dis}, τ_{ch}) pairs over the 5 charge flowrate factors were simulated to determine the grid cost reduction achieved by each configuration and subsequently identify the flowrate factor which maximized the cost reduction for each (τ_{dis}, τ_{ch}) pair. The results are thus once again presented in terms of this maximum grid cost reduction and the flowrate factor enabling the maximum cost reduction for each (τ_{dis}, τ_{ch}) pair.

4.2.1. Optimal TEGS capacity

Fig. 8 shows the maximum cost reduction achieved for the NE grid across the (τ_{dis}, τ_{ch}) pairs analyzed and the optimal flowrate factor which produced the maximum grid cost reduction for each pair. Additionally, Fig. F.17 in Appendix F.2 illustrates the respective installed energy capacities. Fig. G.21 in Appendix G.2 presents analogous results for the TX grid.

Fig. 8 illustrates that for the NE grid, no improvement to charge uniformity, i.e., ff_{ch} = 1, is optimal for TEGS systems with small rated charge durations while a significant improvement in charge uniformity, i.e., ff_{ch} >> 1 is optimal for TEGS systems with large rated charge durations. A similar trend is observed for the TX grid, as illustrated in Fig. G.21. Thus, as with constant-power discharging, the optimality of a flowrate factor seems to be more dependent on the TEGS configuration than the grid characteristics, and the improvement in charge uniformity offered by ff_{ch} > 1 appears to outweigh the associated increase in cost only for TEGS systems with a large τ_{ch}, especially for large τ_{dis} values.

The interpretation of this observation is analogous to that in the constant-power discharging analysis and can be explained in terms of the differences in percentage increase in total CAPEX with rising flowrate factors across TEGS configurations. Fig. 9 illustrates that the contribution of the charging infrastructure to the total CAPEX decreases with increasing rated charge duration and as a direct consequence, the percentage rise in total CAPEX for a given increase in flowrate factor, i.e., for an identical rise in $CAPEX_{ch}$, is lower for systems with large rated charge durations.

There is once again a threshold for this percentage increase in total CAPEX with increasing flowrate factor beyond which the improvement in performance offered by the higher maximum flowrate does not make up for the associated increase in cost. Based on the simulations performed, the value of this threshold seems to be approximately 0.3 % with a minor dependence on system configuration and grid characteristics as before. Unlike in the constant-power discharging analysis where either 1 or 1.8 was always the optimal ff_{dis}, each of the considered ff_{ch} values proves to be optimal for different systems. As hypothesized in the discharging analysis, the optimal flowrate factor increases with decreasing contribution of $CAPEX_{ch}$ to $CAPEX_{tot}$. This is because

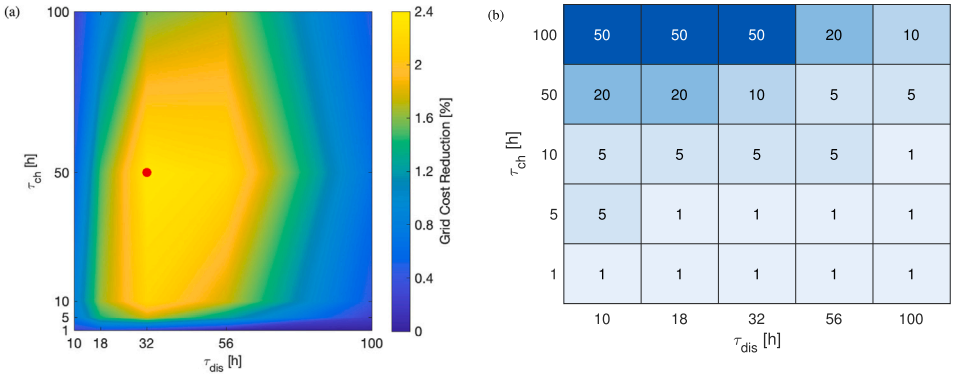

Fig. 8. (a) Maximum grid cost reduction and (b) the respective optimal ff_{ch} enabling maximum grid cost reduction across TEGS configurations for the NE grid. The colorbar in (a) ranges from 0 % to 2.4 %. The (τ_{dis} = 32 h, τ_{ch} = 50 h, ff_{ch} = 10) system produces the maximum cost reduction of 2.4 % and has been highlighted in red.

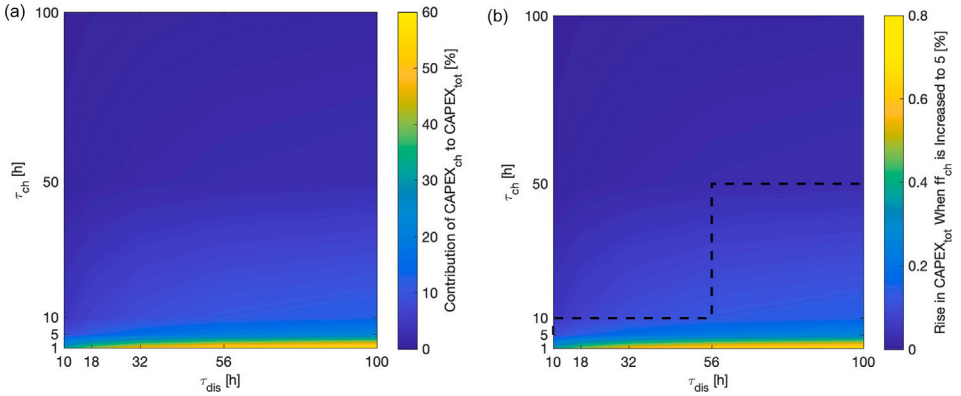

Fig. 9. (a) Contribution of $CAPEX_{ch}$ to $CAPEX_{tot}$ and (b) the rise in $CAPEX_{tot}$ when ff_{ch} is increased from 1 to 5 across TEGS configurations. The colorbar in (a) ranges from 0 % to 60 % and that in (b) from 0 % to 0.8 %. The dotted line in (b) splits the plot into two halves wherein for configurations below the line, $ff_{ch} = 1$ is optimal because the rise in $CAPEX_{tot}$ when ff_{ch} is increased to 5 exceeds the threshold for $ff_{ch} = 5$ to be optimal.

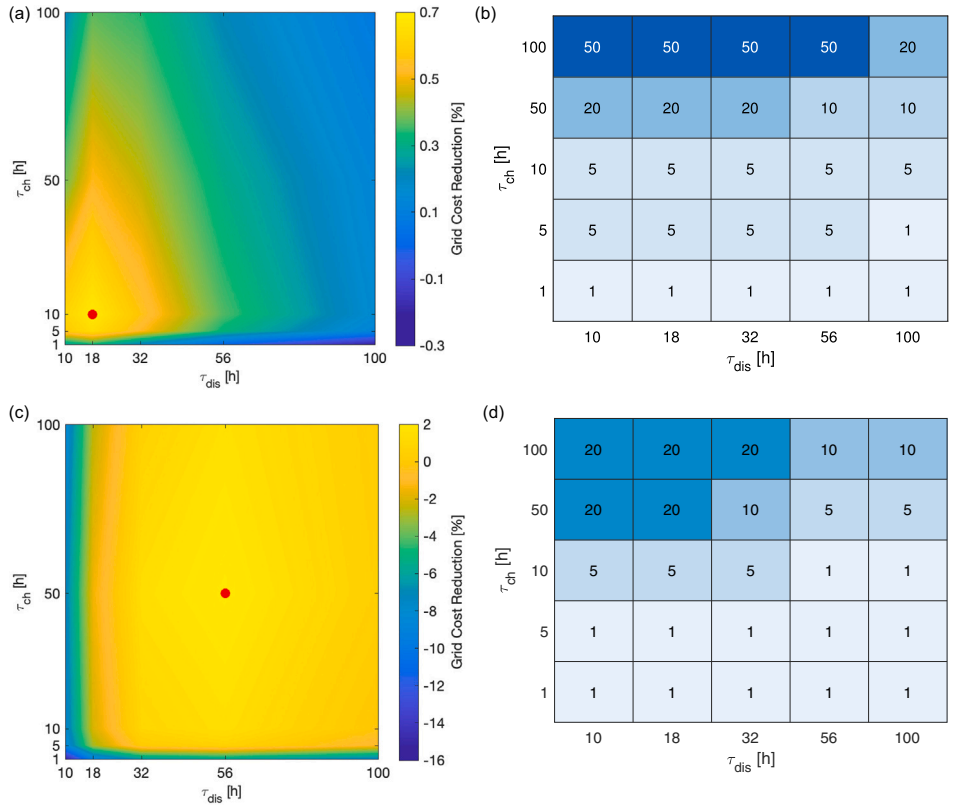

Fig. 10. (a) Maximum grid cost reduction and (b) the respective optimal ff_{ch} enabling maximum grid cost reduction across TEGS configurations for the NE grid when TEGS installed capacity is fixed at 20 GWh. (c) Maximum grid cost reduction and (d) the respective optimal ff_{ch} enabling maximum grid cost reduction across TEGS configurations for the NE grid when TEGS installed capacity is fixed at 400 GWh. The colorbar in (a) ranges from -0.3 % to 0.7 % and that in (c) from -16 % to 2 %. The ($\tau_{dis} = 18$ h, $\tau_{ch} = 10$ h, $ff_{ch} = 5$) and ($\tau_{dis} = 56$ h, $\tau_{ch} = 50$ h, $ff_{ch} = 5$) systems produce the maximum cost reductions of 0.7 % and 2.1 % when capacity is underbuilt and overbuilt respectively and have been highlighted in red. Note the shorter duration systems producing greater cost reductions when capacity is underbuilt and the longer duration systems producing greater cost reductions when capacity is overbuilt.

when the contribution of the charging infrastructure to the total CAPEX is lower, the percentage rise in the total CAPEX for the same rise in the flowrate factor will be lower. This trend is visible here although the range of ff_{ch} values analyzed is even coarser than the ff_{dis} range because $CAPEX_{tot}$ increases only marginally with ff_{ch}.

It is also observed that with constant-power charging incorporated into TEGS design, the global optimum for the NE grid shifts from installing a ($\tau_{dis} = 32$ h, $\tau_{ch} = 50$ h) system which produced a cost reduction of 2.1 % to installing a ($\tau_{dis} = 32$ h, $\tau_{ch} = 50$ h, $ff_{ch} = 10$) system generating a cost reduction of 2.4 % while the global optimum for the TX grid shifts from installing a ($\tau_{dis} = 18$ h, $\tau_{ch} = 10$ h) system which produced a cost reduction of 1.3 % to installing a ($\tau_{dis} = 18$ h, $\tau_{ch} = 10$ h, $ff_{ch} = 5$) system generating a cost reduction of 1.4 %, indicating constant-power charging is beneficial for both the NE and TX grids. The minute increase in $CAPEX_{tot}$ with ff_{ch} is the reason why constant-power charging is able to offer additional value for both

Table 2
Summary of key performance outcomes and associated TEGS configurations.

Performance outcome	TEGS configuration	Grid cost reduction
Maximum grid cost reduction for the NE grid when optimal capacity is built	(τ_{dis} = 32 h, τ_{ch} = 50 h, ff_{ch} = 10)	2.4 %
Maximum grid cost reduction for the NE grid when capacity is underbuilt	(τ_{dis} = 18 h, τ_{ch} = 10 h, ff_{ch} = 5)	0.7 %
Maximum grid cost reduction for the NE grid when capacity is overbuilt	(τ_{dis} = 56 h, τ_{ch} = 50 h, ff_{ch} = 5)	2.1 %
Maximum grid cost reduction for the TX grid when optimal capacity is built	(τ_{dis} = 18 h, τ_{ch} = 10 h, ff_{ch} = 5)	1.4 %
Maximum grid cost reduction for the TX grid when capacity is underbuilt	(τ_{dis} = 18 h, τ_{ch} = 10 h, ff_{ch} = 10)	0.8 %
Maximum grid cost reduction for the TX grid when capacity is overbuilt	(τ_{dis} = 18 h, τ_{ch} = 10 h, ff_{ch} = 5)	1.4 %
Maximum marginal grid cost reduction for the NE grid	(τ_{dis} = 32 h, τ_{ch} = 50 h, ff_{ch} = 50)	0.58 [USD/USD]
Maximum marginal grid cost reduction for the TX grid	(τ_{dis} = 32 h, τ_{ch} = 10 h, ff_{ch} = 5)	0.76 [USD/USD]

the NE and TX grids at the same rated durations deemed optimal in Appendix E.

Finally, as with constant-power discharging, the analysis of marginal grid cost reduction has been presented in Appendix H.2.

4.2.2. Under/ overbuilt TEGS capacity

Fig. 10 shows the maximum cost reduction achieved for the NE grid across the (τ_{dis}, τ_{ch}) pairs analyzed and the optimal flowrate factor which produced the maximum grid cost reduction for each pair when the TEGS capacity was underbuilt and overbuilt. Fig. G.22 in Appendix G.2 presents analogous results for the TX grid. The installed capacities were the same as those in the discharging analysis since the minimum and maximum optimal capacities were also similar to those in the discharging analysis, as illustrated in Fig. F.17 in Appendix F.2 for the NE grid and Fig. G.21(c) in Appendix G.2 for the TX grid.

The observations from this analysis are analogous to those from constant-power discharging. Fig. 10 illustrates that for the NE grid, when TEGS capacity is underbuilt (overbuilt), the optimal flowrate factor increases (decreases) compared to that observed previously for some configurations. As before, this is because a higher (lower) percentage increase in $CAPEX_{tot}$ with ff_{ch} is withstood for the associated performance improvement when TEGS capacity is underbuilt (overbuilt) due to increased (decreased) cycling. Additionally, it is observed that when TEGS capacity is underbuilt (overbuilt), shorter (longer) duration systems produce greater cost reductions. Once again, this is because of the changing system-level behavior of TEGS with capacity and configuration. A similar trend is observed for the TX grid, as illustrated in Fig. G.22.

Table 2 summarizes the main findings from the analysis of TEGS with constant-power charging.

4.3. Analysis of TEGS with oversized energy storage

The aim of this analysis was to determine the value of oversizing the TEGS energy storage to the grid and identify the optimal TEGS configuration when oversized storage is incorporated into the design. The 100 unique TEGS systems, represented by (τ_{dis}, τ_{ch}, s) triplets, obtained by sweeping the 25 (τ_{dis}, τ_{ch}) pairs over the 4 oversizing factors were simulated to determine the grid cost reduction achieved by each configuration and subsequently identify the oversizing factor which maximized the cost reduction for each (τ_{dis}, τ_{ch}) pair. The results are presented in terms of the *additional* grid cost reduction enabled by a particular oversizing factor compared to a larger one for each (τ_{dis}, τ_{ch}) pair.

Fig. 11 shows that grid cost increases as s increases for all (τ_{dis}, τ_{ch}) pairs for the NE grid with similar observations for the TX grid as illustrated in Fig. G.23 in Appendix G.3. So, oversizing the energy storage

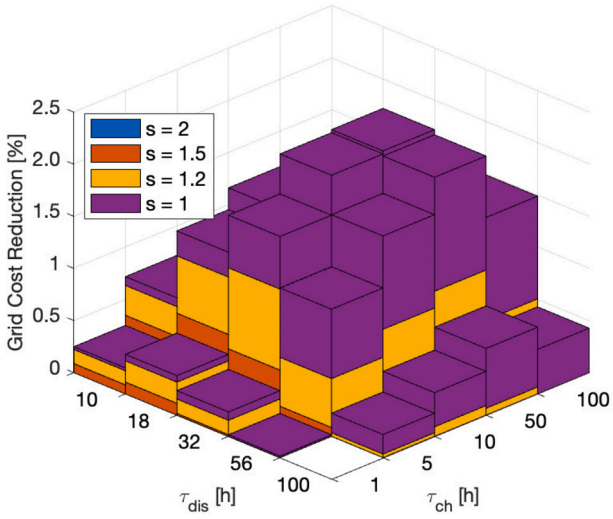

Fig. 11. Grid cost reduction across TEGS configurations for the NE grid at different oversizing levels. Each layer of a stack represents the *additional* cost reduction achieved for a particular s compared to the layer below thus illustrating how the grid cost reduction is higher at lower s for all TEGS configurations. The (τ_{dis} = 32 h, τ_{ch} = 50 h, s = 1) system produces the maximum cost reduction of 2.1 %.

to prevent TEGS systems from operating in low-SOC regimes, in turn enabling a rather constant discharge power, does not provide any value to the grid since the increase in CPE associated with building up excess unused storage capacity far outweighs the value of the discharge power uniformity it offers. Thus, designing TEGS systems with oversized energy storage does not shift the optimal configurations away from those observed for TEGS systems without any performance improvement strategies discussed in Appendix E.

5. Conclusions and outlook

Here, we developed realistic, physics-based, nonlinear TEGS models and subsequently incorporated them into GenX. These models were used to analyze the benefits of certain performance improvement strategies devised to enable a constant discharge power from TEGS, as preferred by utilities, and fast charging capability, to fully utilize cheap, excess electricity. Constant-power discharging realized by progressively increasing the HTF flowrate to higher-than-nominal values and using more of the power block as the graphite storage block cools during discharging was found to enable grid cost reduction when implemented

in TEGS systems such that the rise in $CAPEX_{tot}$ associated with expanded infrastructure can be limited to 5 %. Constant-power charging enabled by progressively increasing the HTF flowrate to higher-than-nominal values during charging as the graphite storage block heats up provides cost benefits when implemented in TEGS systems such that the rise in $CAPEX_{tot}$ associated with expanded infrastructure can be limited to 0.3 %. Oversizing the energy storage such that the SOC never drops below a pre-defined value to in turn enable an approximately constant discharge power was found to offer no grid cost reduction due to the increased costs associated with building up unused capacity outweighing the benefit of an almost constant discharge power.

A limitation of this work is the analysis of discrete TEGS configurations rather than the analysis of a continuous design space due to the lack of analytical formulations for TEGS discharge and charge behaviors. Thus, the first recommendation for future research is to perform simulations for a finer range of maximum (dis)charge flowrates to determine with greater accuracy what the threshold for the percentage increase in $CAPEX_{tot}$ with maximum (dis)charge flowrates is beyond which a higher-than-nominal flowrate would no longer be beneficial, and in turn determine the global optimal TEGS configuration with greater accuracy. The second recommendation is to develop GenX incorporable analytical models of TEGS discharge and charge behaviors to replace the data-driven models developed in this study. A third recommendation would be to combine constant-power discharging and charging in the same system to determine what the optimal configuration would be for such a TEGS design and uncover any synergistic effects. Finally, a more expansive study involving the analysis of numerous emerging TES technologies could be performed such that the optimal capacity mix and operational decisions when different competing technologies are available to be installed on the grid can be determined. Such an analysis could be performed with the framework developed in this study after developing cost estimates and (dis)charge models specific to each relevant TES technology.

CRediT authorship contribution statement

Ashwin Sandeep: Writing – review & editing, Writing – original draft, Visualization, Validation, Project administration, Methodology, Investigation, Formal analysis, Data curation, Conceptualization. **Shomik Verma:** Writing – review & editing, Visualization, Validation, Supervision, Project administration, Methodology, Funding acquisition, Data curation, Conceptualization. **Kyle Buznitsky:** Writing – review & editing, Validation, Supervision, Project administration, Methodology, Conceptualization. **Asegun Henry:** Writing – review & editing, Validation, Supervision, Resources, Project administration, Methodology, Funding acquisition, Conceptualization.

Declaration of competing interest

The authors declare the following financial interests/personal relationships which may be considered as potential competing interests:

Shomik Verma reports financial support was provided by National Science Foundation Graduate Fellowship. Asegun Henry reports a relationship with Fourth Power that includes: board membership and employment. If there are other authors, they declare that they have no known competing financial interests or personal relationships that could have appeared to influence the work reported in this paper.

Acknowledgements

A.S. would like to thank the Heyning-Roelli Foundation for financially supporting the master thesis leading to this publication. The authors would also like to thank Ruaridh Macdonald at the MIT Energy Initiative, Massachusetts Institute of Technology and Odin Foldvik Eikeland at the Department of Physics and Technology, UiT – The Arctic University of Norway for their valuable support and feedback during this project. *Funding: This material is based on work supported by the National Science Foundation Graduate Research Fellowship under Award No. 2141064.*

Appendix A. COMSOL modeling of TEGS

COMSOL Multiphysics® was used for the numerical modeling of TEGS. A TEGS unit was modeled as a cylindrical graphite block with a single channel for Sn flow embedded within, since placing numerous channels in parallel gives equivalent thermal (and therefore (dis)charge) performance. Low-quality graphite, characterized by a thermal conductivity of 10 W/mK, a specific heat capacity of 2000 J/kgK and a density of 1700 kg/m^3, was used as the storage medium. Liquid Sn, characterized by a thermal conductivity of 60–65 W/mK, a specific heat capacity of 247–250 J/kgK, a density of 4800 kg/m^3 and a dynamic viscosity of 0.001 Pa.s, was used as the HTF. Ranges for material properties indicate temperature dependence (in the range 1900 °C – 2400 °C).

An axially symmetric 2D model with an adiabatic outer boundary was used for the simulation. Additionally, constant discharge and charge efficiencies of 0.4 and 0.99 respectively and a laminar HTF flow (due to the insignificant effect of turbulence on heat transfer) were assumed. The relevant geometries and HTF flowrate were optimized to minimize pressure drop while maximizing discharge uniformity for a particular storage duration. As an example, for a TEGS unit with τ_{dis} = 30 h, a graphite block of diameter 0.2 m and length 10 m, an embedded channel of diameter 0.02 m and an HTF flowrate of 0.04 kg/s were deemed optimal. Further details about the modeling approach can be found in [9].

Appendix B. Calculation of TEGS CPE, CPP_{dis} and CPP_{ch}

This cost computation assumes a TEGS unit with a storage capacity of 1 GWh and a discharge power capacity of 100 MW which influence the CPE and CPP_{dis} respectively. Since CPP_{ch} is independent of charge power capacity, the value computed here is applicable to all TEGS systems. Additionally, maximum and minimum operating temperatures of 2400 °C and 1900 °C respectively, a daily heat loss of 3 % and discharge and charge efficiencies of 0.5 and 0.99 respectively are assumed.

CPE: The storage infrastructure cost includes the costs of the following elements:

- Storage medium, graphite
- HTF, Sn
- Graphite felt, alumina and fibreglass insulation layers for the storage blocks
- Inert containment for the storage blocks
- Concrete base for the storage blocks
- Cooling for the concrete base and
- Construction.

The costs of the graphite storage medium (1.84 $/kWh-th), Sn HTF (3.46 $/kWh-th), insulation layers (1.37 $/kWh-th) and concrete base (0.25 $/kWh-th) are calculated using the respective volumes (derived from the energy capacity of the TEGS unit) and cost per unit volume. The cooling cost (0.03 $/kWh-th) is computed from the heat loss through the tank base and cost of cooling per unit power. Finally, the cost of the inert containment (0.05 $/kWh-th) and construction cost (2.27 $/kWh-th) are derived from existing cost models [8]. This results in a CPE of 9.3 $/kWh-th.

CPP_{dis}: The discharging infrastructure cost includes the costs of the following elements:

- TPV power block

  - TPV cells
  - Cooling for the TPV cells
  - Inverter
  - Tungsten foil used as emitter
  - Graphite pipes and headers for transporting Sn
  - Graphite felt, alumina and fibreglass insulation layers for the emitter and pipes
- Control system
- Pumping system and
- Construction.

The costs of the TPV cells (¢15.8/W-e), W foil (¢4.4/W-e), graphite pipes and headers (¢4.1/W-e) and insulation layers (¢0.2/W-e) are calculated using the respective areas (derived from the discharge power capacity of the TEGS unit and TPV cell power density) and cost per unit area. The pumping system cost (¢0.01/W-e) is computed assuming the use of two 2000 kg graphite pumps and 100 m of graphite piping and multiplying the respective masses by the cost per unit mass. Finally, the inverter (¢14.6/W-e), cooling (¢14.6/W-e), control system (¢2.2/W-e) and construction costs (¢0.6/W-e) are derived from existing cost models [8]. This results in a CPP_{dis} of ¢56.7/W-e.

***CPP*$_{ch}$**: The charging infrastructure cost includes the costs of the following elements:

- Heater
  - Heater elements
  - Heater controller
  - Graphite pipes and headers for transporting Sn
  - Graphite felt, alumina and fibreglass insulation layers for the heater and
- Pumping system.

The costs of the heater elements (¢0.19/W-e), heater controller (¢0.92/W-e), graphite pipes and headers (¢0.55/W-e) and insulation layers (¢0.04/W-e) are derived from existing cost models [8] while the pumping system cost (¢0.01/W-e) is computed as before. This results in a CPP_{ch} of ¢1.7/W-e.

Appendix C. Variation of Sn outlet temperature with SOC for constant-power dis(charging)

See Fig.C.12.

Appendix D. Incorporation of TEGS into GenX

D.1. Previous implementation

The discharging and charging powers available from a storage resource at each time instant (each hour of the simulated year) are an input required by GenX so that it can determine the maximum discharging and charging powers the grid can request from the respective storage resource at a particular time instant [20]. These constraints are mathematically represented as

$$\Theta_{y,t} \leq P_{dis,el,y,t}, \tag{D.1}$$

$$\Pi_{y,t} \leq P_{ch,el,y,t}, \tag{D.2}$$

where $P_{dis,el,y,t}$ and $P_{ch,el,y,t}$ are the instantaneous electrical discharge and charge powers available from a storage resource y at time step t and $\Theta_{y,t}$ and $\Pi_{y,t}$ are the discharge and charge powers requested by the grid from that storage resource at that time step.

The TEGS models previously implemented in GenX represent best-case and worst-case TEGS behavior [19]. For the best-case TEGS, it is assumed that the dis(charge) powers available are independent of SOC and are always equal to the installed capacities. Thus, Eqs. (D.1) and (D.2) become

$$\Theta_{TEGS,t} \leq \Delta_{dis,TEGS}, \tag{D.3}$$

$$\Pi_{TEGS,t} \leq \Delta_{ch,TEGS}, \tag{D.4}$$

where $\Delta_{dis,TEGS}$ and $\Delta_{ch,TEGS}$ are the discharge and charge power capacities of TEGS installed in the grid which are linked by Eq. (8).

For the worst-case TEGS, it is assumed that the dis(charge) powers available from TEGS vary linearly with SOC. Thus, Eqs. (D.3) and (D.4) are modified as

$$\Theta_{TEGS,t} \leq \Delta_{dis,TEGS} SOC, \tag{D.5}$$

$$\Pi_{TEGS,t} \leq \Delta_{ch,TEGS}(1 - SOC). \tag{D.6}$$

These best-case and worst-case TEGS behaviors are visualized in Fig. D.13 through plots showing the variation of maximum available discharge and charge powers with SOC for a hypothetical TEGS system.

A point of note is that SOC is not a GenX decision variable. Thus, it needs to be represented in terms of the energy capacity and the actual energy stored at a particular time instant, which are in fact decision variables, when it is to be used in a constraint. Thus, Eqs. (D.5) and

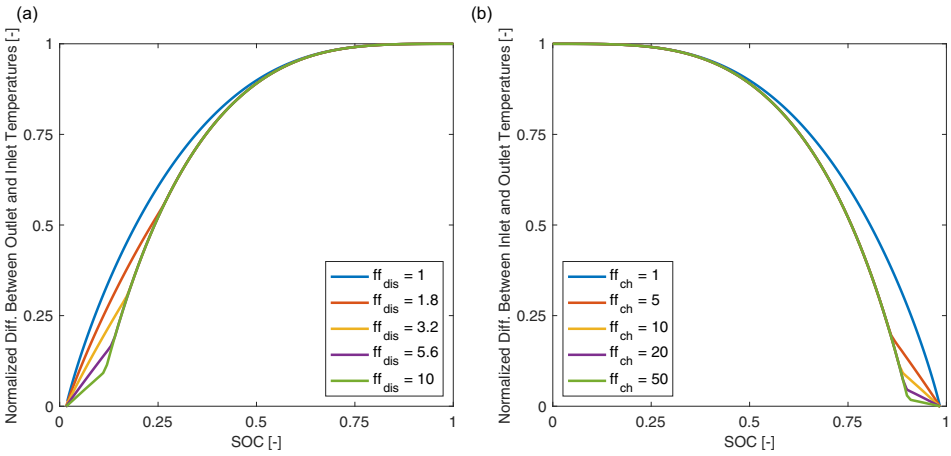

Fig. C.12. Variation of Sn outlet temperature with SOC for (a) a TEGS system with τ_{dis} = 10 h for increasing ff_{dis} values and (b) a TEGS system with τ_{ch} = 10 h for increasing ff_{ch} values.

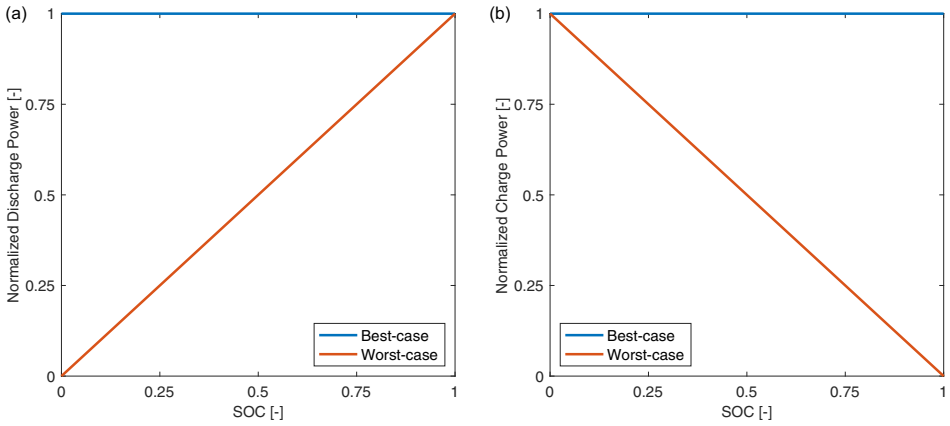

Fig. D.13. (a) Discharge and (b) charge behaviors of hypothetical best-case and worst-case TEGS systems.

(D.6) were modified using relationships shown in Eq. (8) before they were incorporated into GenX as

$$\Theta_{TEGS,t}\frac{\tau_{dis}}{\eta_{dis}} \leq \Gamma_{TEGS,t-1}, \tag{D.7}$$

$$\Pi_{TEGS,t}\tau_{ch}\eta_{ch} \leq \Delta_{en,TEGS} - \Gamma_{TEGS,t-1}, \tag{D.8}$$

where $\Gamma_{TEGS,t-1}$ is the energy stored in TEGS in the previous time step which determines the powers available in the current time step and $\Delta_{en,TEGS}$ is the installed energy capacity of TEGS.

Since the constraints defining the (dis)charge powers available from the best-case TEGS are independent of TEGS rated durations, its implementation in GenX does not require the explicit definition of these rated durations. Thus, rather than having to simulate discrete TEGS systems characterized by their unique rated durations, the optimal rated durations could be derived as outputs based on the optimal TEGS capacities installed, using Eq. (8), as is done in [19]. However, this is not the case for the worst-case TEGS where the constraints on powers available are indeed a function of the rated durations which means that leaving them undefined would result in a nonlinear problem. Since the authors of [19] wanted to preserve the linearity of the overall GenX model, the optimal rated durations (for TEGS systems characterized by a particular operating temperature and daily heat loss) derived from the analysis of the best-case TEGS were used to simulate discrete worst-case TEGS systems. This is less than ideal since the optimal configuration for a particular combination of TEGS operating temperature and daily heat loss need not be the same for best and worst-case TEGS systems.

D.2. Current implementation

Since the actual behavior of TEGS lies somewhere in between those embodied by the existing models, the previous implementation of TEGS in GenX was required to be modified in the interest of enhancing modeling accuracy. Additionally, the performance improvement strategies discussed in Section 2 could only be evaluated using more complex models.

Physics-based models for the variation of TEGS dis(charge) powers with SOC were required to be developed to accurately capture the actual TEGS behavior. Such models could then be used to implement the constraints in Eqs. (D.1) and (D.2) as

$$\Theta_{TEGS,t} \leq \Delta_{dis,TEGS} f(SOC), \tag{D.9}$$

$$\Pi_{TEGS,t} \leq \Delta_{ch,TEGS} f(SOC), \tag{D.10}$$

where $f(SOC)$ represents the models for the variation of normalized (dis)charge powers with SOC.

Three approaches were identified to develop the new, more realistic TEGS models using the available COMSOL data, namely (a) Linear interpolation (LI), (b) Piece-wise linear (PL) fitting and (c) Piece-wise nonlinear (PNL) fitting. Although the incorporation of the models developed using these strategies into GenX seemed reasonably straightforward, unanticipated issues arose.

A linearization of the constraints in Eqs. (D.9) and (D.10) in terms of the GenX decision variables for implementing the LI and PL models was impossible due to the use of the *interpolation* function and *if-else* statements. Thus, in addition to the PNL models which were nonlinear in SOC (and so in $\Delta_{en,TEGS}$ and $\Gamma_{TEGS,t-1}$) by definition, the LI and PL models were also nonlinear when implemented in GenX, resulting in a nonlinear optimization problem for all three model types. As a result, performing simulations with all three types of models required the replacement of the standard Gurobi solver [23] used in [19] with the Ipopt solver [24] specifically developed for nonlinear optimization problems. However, when simulations were indeed run following the solver change, they failed to converge. The reason for this was ascertained to be the fact that although Ipopt accepts non-differentiable functions like *interpolation* and *if-else*, it assumes that all functions are smooth and twice differentiable which sometimes results in non-convergence when this is not the case. This meant that none of the three strategies identified for incorporating the new models into GenX were practically feasible and a new modeling approach was necessary.

The final modeling strategy used for the development of the physics-based models for the variation of (dis)charge powers with SOC involved using a single nonlinear function rather than a piece-wise approximation since this would avoid the need for any non-differentiable functions when incorporating the TEGS models into GenX. However, a drawback of this strategy was the increased data fitting error compared to the previous approaches.

Two nonlinear functions which enabled a relatively low data fitting error while not being unnecessarily complicated were identified. The first was a transformation of the hyperbolic tangent function given by

$$f(SOC) = c\tanh(aSOC + b) + d, \tag{D.11}$$

where a, b, c and d are coefficients identified during the fitting process. This function was appropriate for all discharge curves and most charge curves. The charge curves which could not be accurately modeled using this function were those of TEGS systems with extremely low values of τ_{ch} (e.g. 1 h, such low τ_{dis} values were not studied). For such systems, a linear combination of an exponential and an affine function given by

$$f(SOC) = \exp(aSOC + b) + cSOC + d, \tag{D.12}$$

where a, b, c and d are once again coefficients identified during fitting was used to model the charge curves.

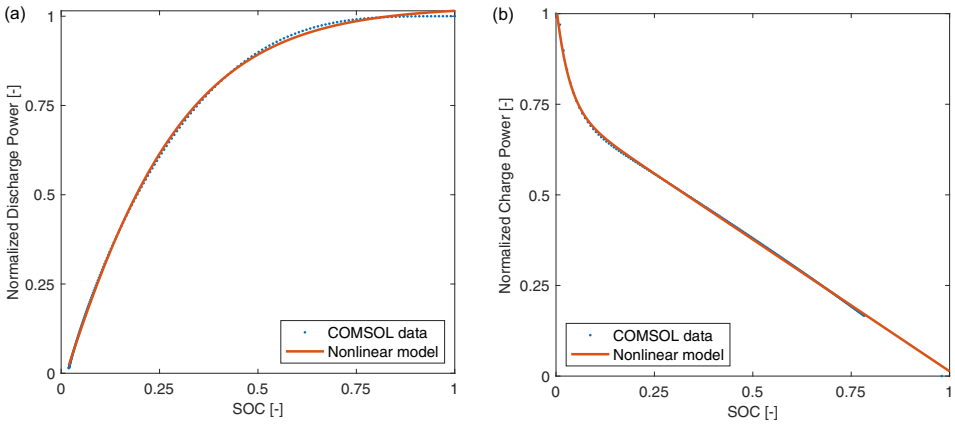

Fig. D.14. Nonlinear models of the (dis)charge behaviors of a TEGS system. (a) Discharge behavior of a ($\tau_{dis} = 10$ h, $ff_{dis} = 1$) TEGS system. (b) Charge behavior of a ($\tau_{ch} = 1$ h, $ff_{ch} = 1$) TEGS system.

These functions enabled RMSE values around 0.01–0.02 which, although an order of magnitude higher than the lowest RMSE values provided by certain PNL fitting strategies, were deemed acceptable given the data range of 1 (equivalent to an RMSPE below 5 %). The nonlinear discharge power model for a TEGS system with $\tau_{dis} = 10$ h and $ff_{dis} = 1$ and the nonlinear charge power model for a TEGS system with $\tau_{ch} = 1$ h and $ff_{ch} = 1$ are displayed in Fig. D.14.

These nonlinear models could be seamlessly integrated into GenX and convergence was achieved.

Appendix E. Validation of the nonlinear TEGS models

This analysis is aimed at proving the validity of the simulation results obtained using the new TEGS models. Although the nonlinear TEGS (dis)charge models are expected to offer more accurate results, this validation is necessary because their incorporation into GenX transforms it into a nonlinear optimization model with no global optimality guarantees. The validation is done by comparing the results of this nonlinear optimization with those obtained in [19]. Since the simulation framework employed in both studies is identical, the results can be directly compared.

Fig. E.15 shows the cost reduction achieved for the NE and TX grids across the TEGS configurations analyzed compared to a baseline scenario without TEGS.

In [19], a ($\tau_{dis} = 32.7$ h, $\tau_{ch} = 34.8$ h) TEGS configuration was found to be optimal for the NE grid. This configuration reduced the cost of the grid by around 4 % and 0.4 % for the best-case (dis(charge) powers independent of SOC and always equal to installed capacities) and worst-case (dis(charge) powers linearly varying with SOC) TEGS respectively. Among the TEGS configurations analyzed here, the ($\tau_{dis} = 32$ h, $\tau_{ch} = 50$ h) configuration is optimal since it offers the maximum grid cost reduction of approximately 2.1 %, as can be observed in Fig. E.15.

Analogously, a ($\tau_{dis} = 16.8$ h, $\tau_{ch} = 9.1$ h) TEGS configuration was found to be optimal for the TX grid in [19] with that configuration resulting in a grid cost reduction of around 3 % for the best-case TEGS while not reducing costs compared to the baseline scenario for the worst-case TEGS. Fig. E.15 shows that the ($\tau_{dis} = 18$ h, $\tau_{ch} = 10$ h) configuration is optimal in this analysis and it offers a grid cost reduction of approximately 1.3 %.

Thus, the optimal TEGS configurations determined in this analysis for both grids have rated durations comparable to the optimal rated durations derived in [19]. Moreover, the maximum cost savings achieved here lie between those offered by the best and worst-case TEGS, as would be expected. These serve as confirmation that the results from the nonlinear optimization model are reliable and that the actual TEGS behavior is indeed intermediate between those of the best and worst-case TEGS. Thus, the validity of the new modeling and simulation approach has been established.

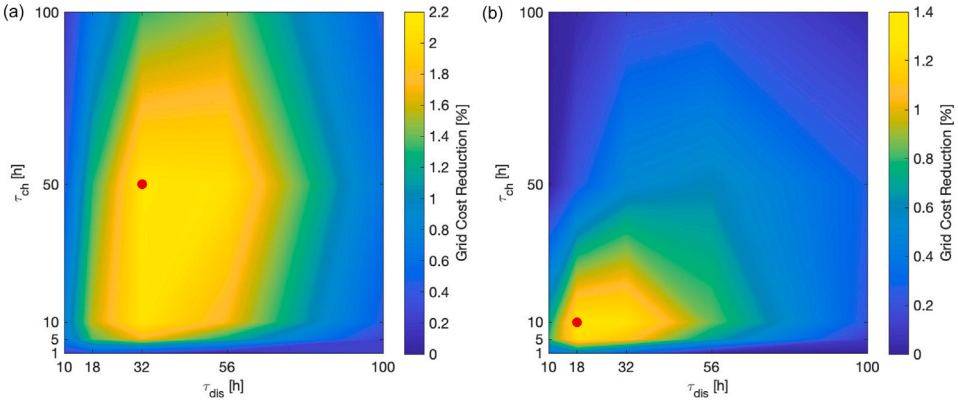

Fig. E.15. Grid cost reduction across TEGS configurations for the (a) NE and (b) TX grids. The colorbar in (a) ranges from 0 % to 2.2 % and that in (b) from 0 % to 1.4 %. The ($\tau_{dis} = 32$ h, $\tau_{ch} = 50$ h) and ($\tau_{dis} = 18$ h, $\tau_{ch} = 10$ h) systems produce the maximum cost reductions of 2.1 % and 1.3 % for the NE and TX grids respectively and have been highlighted in red.

Appendix F. Additional results for the NE grid

F.1. Analysis of TEGS with constant-power discharging

See Fig.F.16.

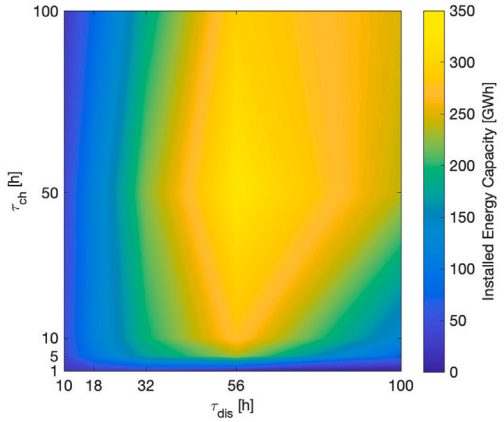

Fig. F.16. Installed energy capacity enabling maximum grid cost reduction across TEGS configurations for the NE grid. The colorbar ranges from 0 GWh to 350 GWh.

F.2. Analysis of TEGS with constant-power charging

See Fig.F.17.

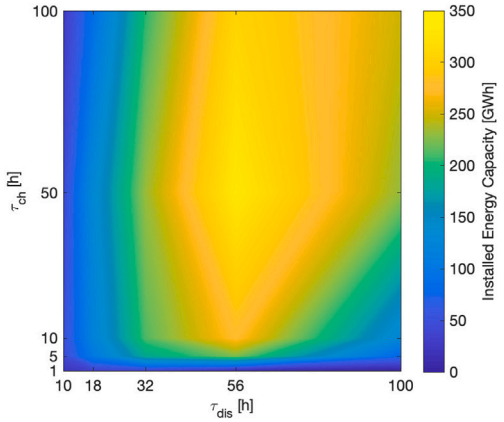

Fig. F.17. Installed energy capacity enabling maximum grid cost reduction across TEGS configurations for the NE grid. The colorbar ranges from 0 GWh to 350 GWh.

Appendix G. Results for the TX grid

G.1. Analysis of TEGS with constant-power discharging

See Fig.G.18, Fig.G.19, Fig.G.20

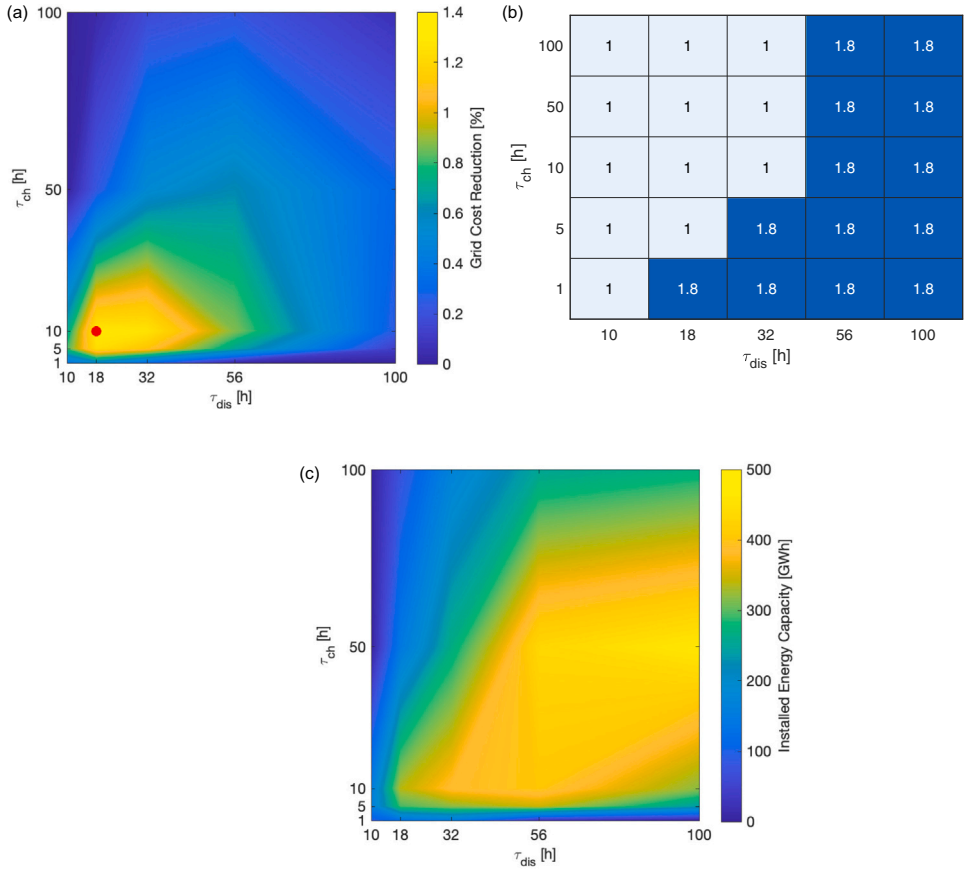

Fig. G.18. (a) Maximum grid cost reduction and the respective (b) optimal ff_{dis} and (c) installed energy capacity enabling maximum grid cost reduction across TEGS configurations for the TX grid. The colorbar in (a) ranges from 0 % to 1.4 % and that in (c) from 0 GWh to 500 GWh. The (τ_{dis} = 18 h, τ_{ch} = 10 h, ff_{dis} = 1) system produces the maximum cost reduction of 1.3 % and has been highlighted in red.

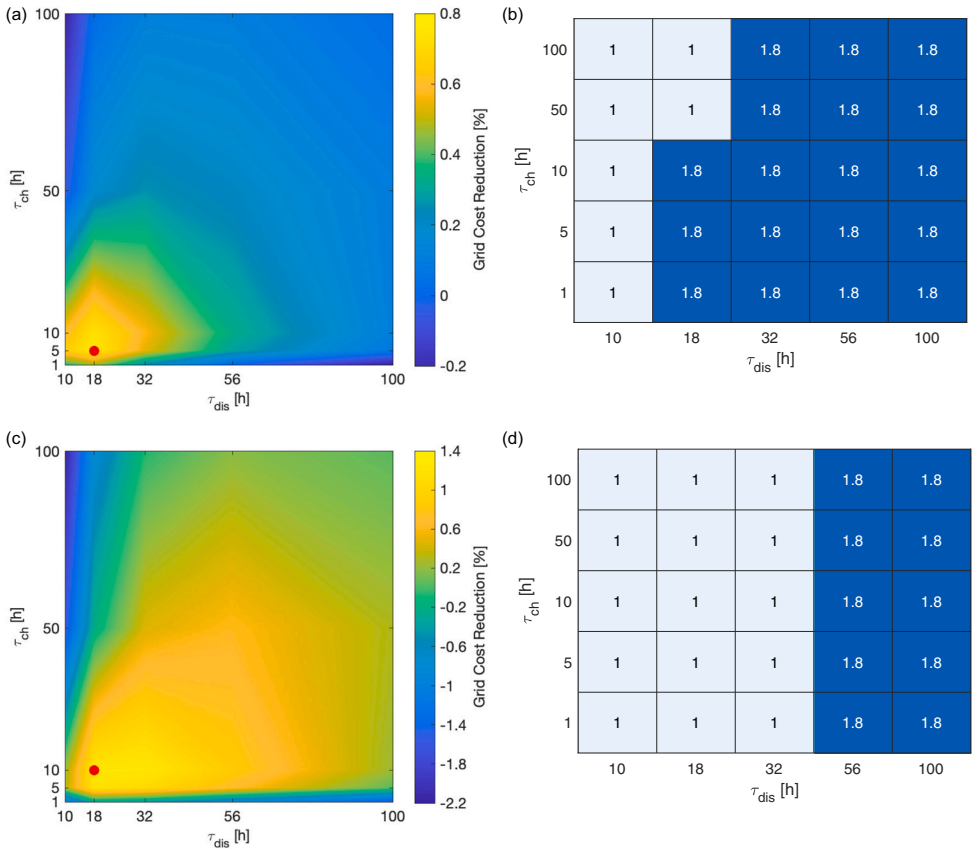

Fig. G.19. (a) Maximum grid cost reduction and (b) the respective optimal ff_{dis} enabling maximum grid cost reduction across TEGS configurations for the TX grid when TEGS installed capacity is fixed at 100 GWh. (c) Maximum grid cost reduction and (d) the respective optimal ff_{dis} enabling maximum grid cost reduction across TEGS configurations for the TX grid when TEGS installed capacity is fixed at 500 GWh. The colorbar in (a) ranges from -0.2 % to 0.8 % and that in (c) from -2.2 % to 1.4 %. The ($\tau_{dis} = 18$ h, $\tau_{ch} = 5$ h, $ff_{dis} = 1.8$) and ($\tau_{dis} = 18$ h, $\tau_{ch} = 10$ h, $ff_{dis} = 1$) systems produce the maximum cost reductions of 0.8 % and 1.3 % when capacity is underbuilt and overbuilt respectively and have been highlighted in red. Note the shorter duration systems producing greater cost reductions when capacity is underbuilt and the longer duration systems producing greater cost reductions when capacity is overbuilt.

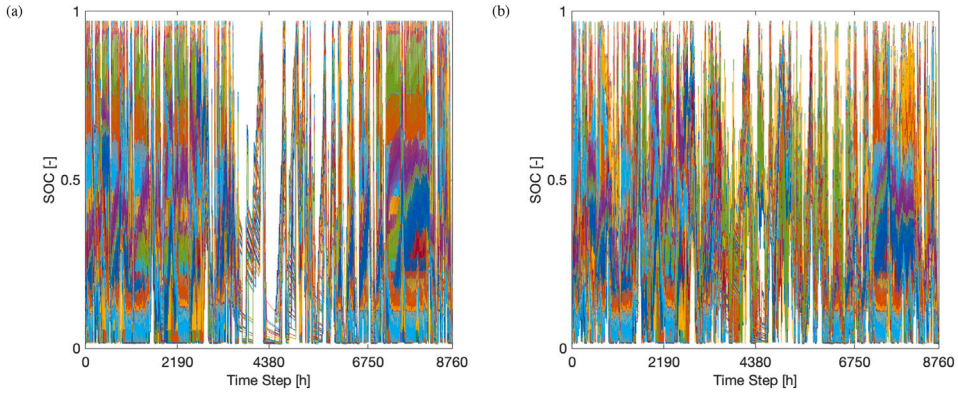

Fig. G.20. SOC profiles of TEGS configurations over the studied year for the TX grid when TEGS capacity is (a) underbuilt (100 GWh) and (b) overbuilt (500 GWh). Note the much higher frequency of SOC cycling between 0 and 1 when capacity is underbuilt.

G.2. Analysis of TEGS with constant-power charging

See Fig.G.21,Fig.G.22.

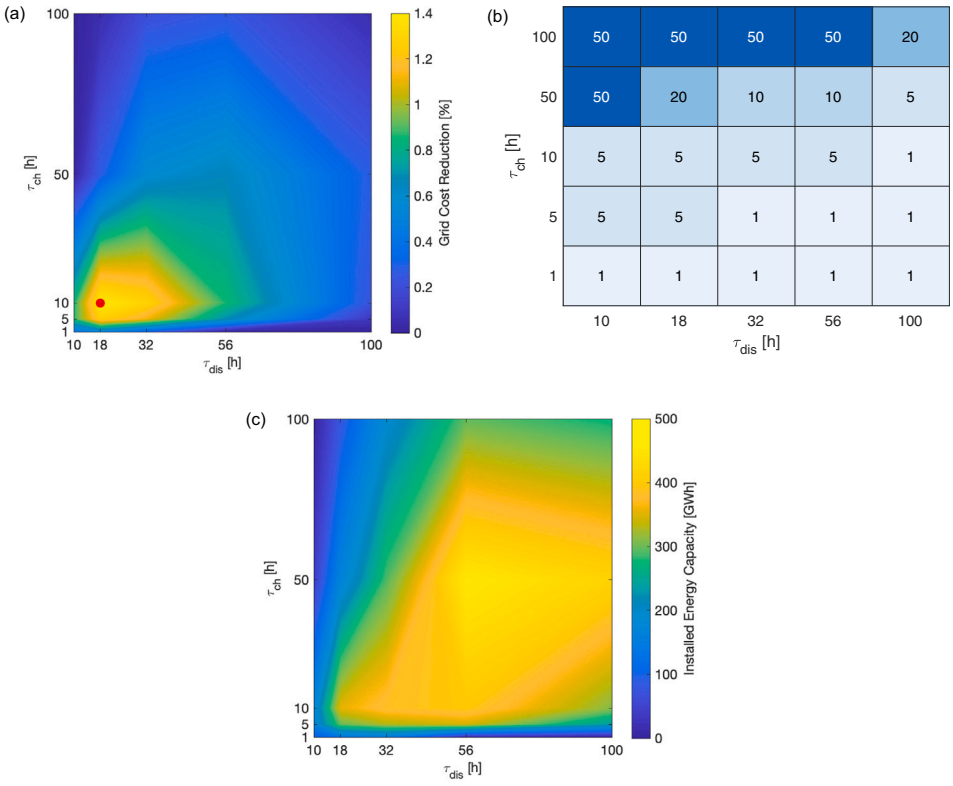

Fig. G.21. (a) Maximum grid cost reduction and the respective (b) optimal ff_{ch} and (c) installed energy capacity enabling maximum grid cost reduction across TEGS configurations for the TX grid. The colorbar in (a) ranges from 0 % to 1.4 % and that in (c) from 0 GWh to 500 GWh. The (τ_{dis} = 18 h, τ_{ch} = 10 h, ff_{ch} = 5) system produces the maximum cost reduction of 1.4 % and has been highlighted in red.

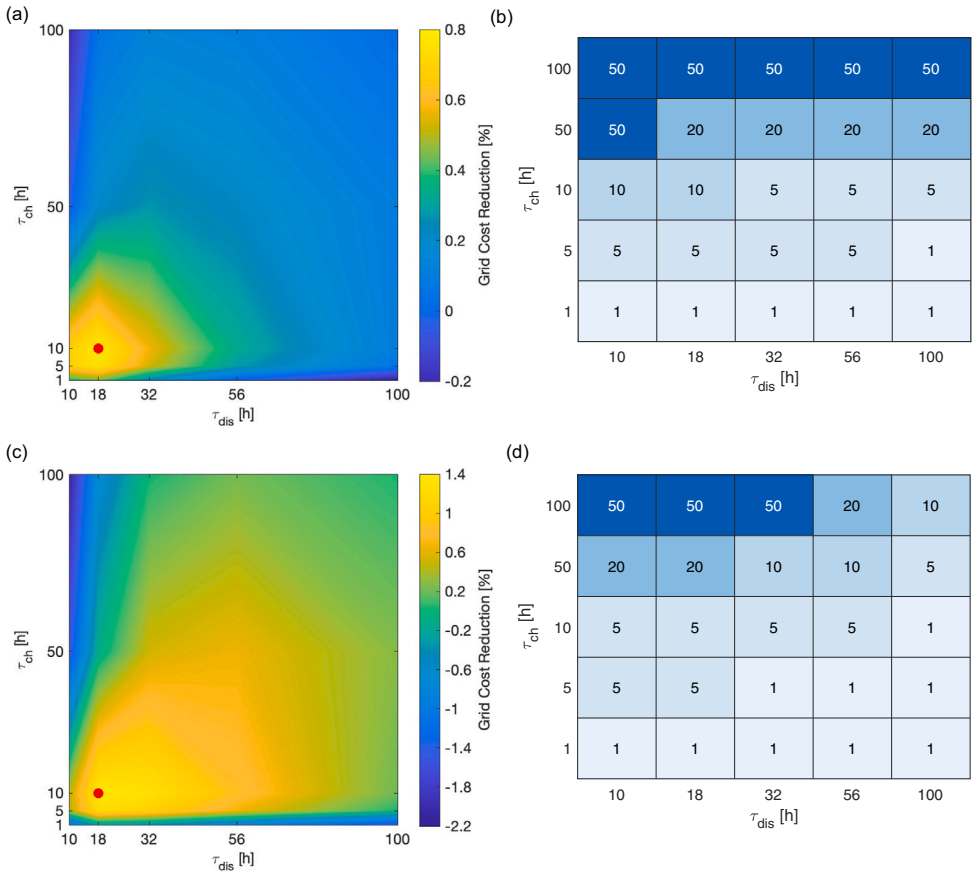

Fig. G.22. (a) Maximum grid cost reduction and (b) the respective optimal ff_{ch} enabling maximum grid cost reduction across TEGS configurations for the TX grid when TEGS installed capacity is fixed at 100 GWh. (c) Maximum grid cost reduction and (d) the respective optimal ff_{ch} enabling maximum grid cost reduction across TEGS configurations for the TX grid when TEGS installed capacity is fixed at 500 GWh. The colorbar in (a) ranges from -0.2 % to 0.8 % and that in (c) from -2.2 % to 1.4 %. The ($\tau_{dis} = 18$ h, $\tau_{ch} = 10$ h, $ff_{ch} = 10$) and ($\tau_{dis} = 18$ h, $\tau_{ch} = 10$ h, $ff_{ch} = 5$) systems produce the maximum cost reductions of 0.8 % and 1.4 % when capacity is underbuilt and overbuilt respectively and have been highlighted in red. Note the shorter duration systems producing greater cost reductions when capacity is underbuilt and the longer duration systems producing greater cost reductions when capacity is overbuilt.

G.3. Analysis of TEGS with oversized energy storage

See Fig.G.23.

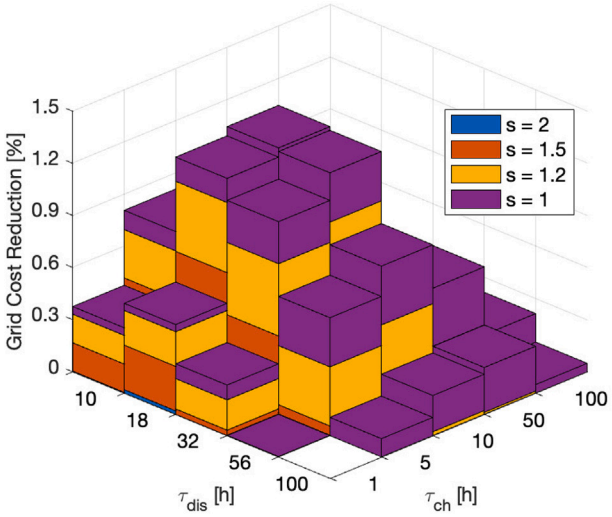

Fig. G.23. Grid cost reduction across TEGS configurations for the TX grid at different oversizing levels. Each layer of a stack represents the *additional* cost reduction achieved for a particular s compared to the layer below thus illustrating how the grid cost reduction is higher at lower s for all TEGS configurations. The ($\tau_{dis} = 18$ h, $\tau_{ch} = 10$ h, $s = 1$) system produces the maximum cost reduction of 1.3 %.

Appendix H. Marginal grid cost reduction

Marginal grid cost reduction has been introduced as an alternative metric to address the reality that unlimited monetary resources are often not available to the investor, meaning the implementation of the TEGS system which maximizes absolute grid cost reduction may often not be possible. In such scenarios, systems that offer the most value for money, i.e., those that maximize grid cost savings per investment cost of TEGS [USD/USD], defined here as marginal grid cost reduction, could be a suitable alternative.

H.1. Analysis of TEGS with constant-power discharging

Fig. H.24 shows the maximum marginal cost reduction achieved for the NE and TX grids across the (τ_{dis}, τ_{ch}) pairs analyzed and the optimal flowrate factor which produced the maximum marginal grid cost reduction for each pair.

Fig. H.24 illustrates that when the metric of interest is changed from absolute grid cost reduction to marginal grid cost reduction, the TEGS configurations which prove optimal also change. For the NE grid, the global optimum would now be installing a (τ_{dis} = 32 h, τ_{ch} = 50 h, ff_{dis} = 1.8) system which provides a marginal grid cost reduction of 0.55 [USD/USD] compared to the marginal grid cost reduction of 0.46 [USD/USD] provided by the (τ_{dis} = 56 h, τ_{ch} = 50 h, ff_{dis} = 1.8) system deemed optimal previously. Similarly, for the TX grid, the global optimum would now be installing a (τ_{dis} = 32 h, τ_{ch} = 10 h, ff_{dis} = 1) system which provides a marginal grid cost reduction of 0.74 [USD/USD] compared to the marginal grid cost reduction of 0.64 [USD/USD] provided by the (τ_{dis} = 18 h, τ_{ch} = 10 h, ff_{dis} = 1) system deemed optimal previously.

It can also be observed that shorter duration systems generally produce greater marginal grid cost reductions than longer duration systems. Shorter duration systems add value to the grid through arbitrage while longer duration ones contribute through grid balancing and firm capacity replacement, as discussed in Sections 4.1 and 4.2. Thus, this observation is indicative of the diminishing returns associated with arbitrage opportunities. It is less capital intensive to derive grid cost savings by utilizing arbitrage opportunities but there is less absolute cost savings to be had. Conversely, it is more capital intensive to derive grid cost savings through grid balancing and firm capacity replacement but there is more absolute cost savings to be had.

H.2. Analysis of TEGS with constant-power charging

Fig. H.25 shows the maximum marginal cost reduction achieved for the NE and TX grids across the (τ_{dis}, τ_{ch}) pairs analyzed and the optimal flowrate factor which produced the maximum marginal grid cost reduction for each pair.

Fig. H.25 once again illustrates that when marginal grid cost reduction is the metric of interest, the optimal TEGS configurations change. For the NE grid, the global optimum would now be installing a (τ_{dis} = 32 h, τ_{ch} = 50 h, ff_{ch} = 50) system which provides a marginal grid cost reduction of 0.58 [USD/USD] compared to the marginal grid cost reduction of 0.57 [USD/USD] provided by the (τ_{dis} = 32 h, τ_{ch} = 50 h, ff_{ch} = 10) system deemed optimal previously. Similarly, for the TX grid, the global optimum would now be installing a (τ_{dis} = 32 h, τ_{ch} = 10 h, ff_{ch} = 5) system which provides a marginal grid cost reduction of 0.76 [USD/USD] compared to the marginal grid cost reduction of 0.66 [USD/USD] provided by the (τ_{dis} = 18 h, τ_{ch} = 10 h, ff_{ch} = 5) system deemed optimal previously. Also, shorter duration

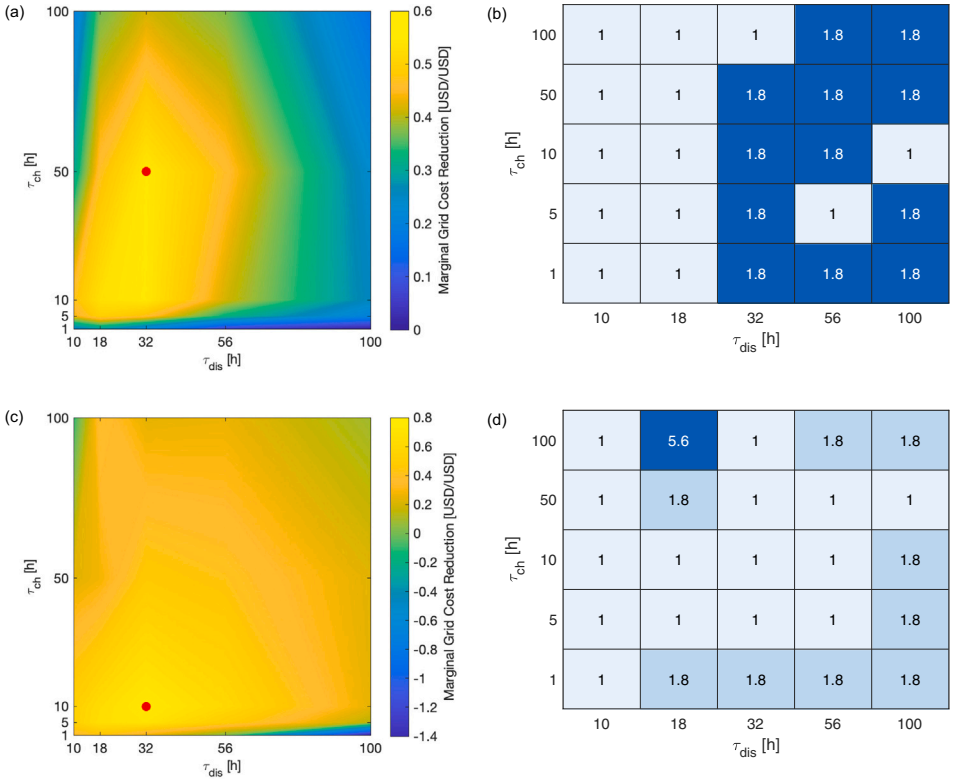

Fig. H.24. (a) Maximum marginal grid cost reduction and (b) the respective optimal ff_{dis} enabling maximum marginal grid cost reduction across TEGS configurations for the NE grid. (c) Maximum marginal grid cost reduction and (d) the respective optimal ff_{dis} enabling maximum marginal grid cost reduction across TEGS configurations for the TX grid. The colorbar in (a) ranges from 0 [USD/USD] to 0.6 [USD/USD] and that in (c) from −1.4 [USD/USD] to 0.8 [USD/USD]. The (τ_{dis} = 32 h, τ_{ch} = 50 h, ff_{dis} = 1.8) and (τ_{dis} = 32 h, τ_{ch} = 10 h, ff_{dis} = 1) systems produce the maximum marginal cost reductions of 0.55 [USD/USD] and 0.74 [USD/USD] for the NE and TX grids respectively and have been highlighted in red.

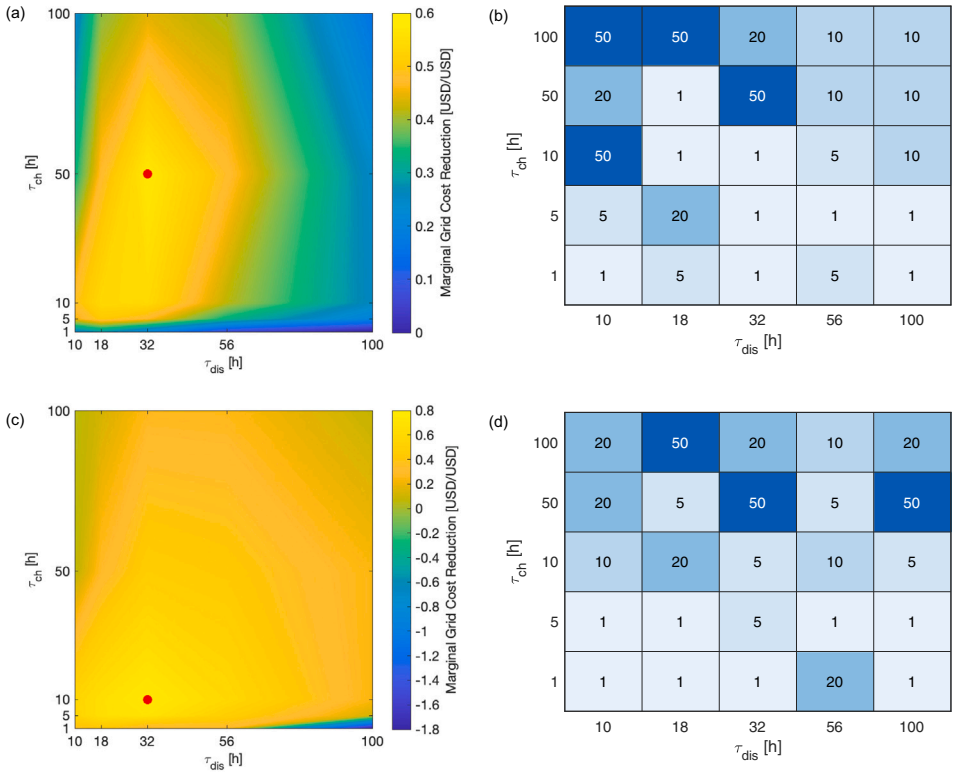

Fig. H.25. (a) Maximum marginal grid cost reduction and (b) the respective optimal ff_{ch} enabling maximum marginal grid cost reduction across TEGS configurations for the NE grid. (c) Maximum marginal grid cost reduction and (d) the respective optimal ff_{ch} enabling maximum marginal grid cost reduction across TEGS configurations for the TX grid. The colorbar in (a) ranges from 0 [USD/USD] to 0.6 [USD/USD] and that in (c) from -1.8 [USD/USD] to 0.8 [USD/USD]. The (τ_{dis} = 32 h, τ_{ch} = 50 h, ff_{ch} = 50) and (τ_{dis} = 32 h, τ_{ch} = 10 h, ff_{ch} = 5) systems produce the maximum marginal cost reductions of 0.58 [USD/USD] and 0.76 [USD/USD] for the NE and TX grids respectively and have been highlighted in red.

systems produce greater cost reductions than longer duration ones as before.

Appendix I. Fixed-budget case study of TEGS with constant-power (Dis)charging

The reality of budget constraints for implementing clean energy technologies on the grid is addressed in this case study which was aimed at understanding how the optimal TEGS configuration changes when only a limited budget is available for implementing TEGS on the grid. Thus, simulations assuming the availability of 50 %, 10 % and 1 % of the total CAPEX required to implement the optimal TEGS configuration in the budget unconstrained scenarios were performed to determine how the optimality shifts in such cases. These simulations were performed for both the NE and TX grids for both constant-power discharging and charging incorporated into TEGS design (i.e., for the 250 unique TEGS systems analyzed across Sections 4.1 and 4.2). While the total CAPEX of each TEGS configuration would be identical for a particular budget scenario, the distribution of this CAPEX among the charging, storage and discharging infrastructures would still depend on the configuration. This is illustrated in Fig. I.26.

In addition to evaluating trends in grid cost reduction as before, the return on investment (ROI) is also studied to determine whether the same configurations would prove optimal for both the grid and the investor.

Fig. I.27 shows the maximum grid cost reduction and maximum ROI across the analyzed TEGS configurations with constant-power discharging for the NE and TX grids.

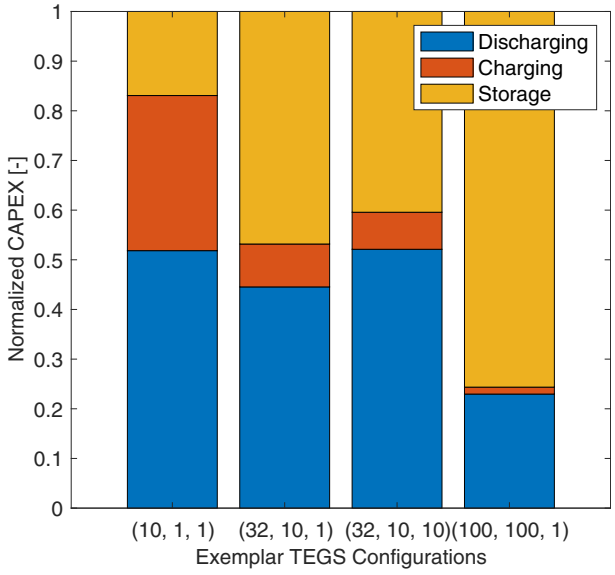

Fig. I.26. Breakdown of the total CAPEX among the charging, storage and discharging infrastructures for some TEGS configurations with constant-power discharging, represented as (τ_{dis}, τ_{ch}, ff_{dis}) triplets. Note how most of the CAPEX is associated with the discharging and charging infrastructures for the (τ_{dis} = 10 h, τ_{ch} = 1 h, ff_{dis} = 1) system due to its small (dis)charge durations while most of the CAPEX is associated with the storage infrastructure for the (τ_{dis} = 100 h, τ_{ch} = 100 h, ff_{dis} = 1) system due to its large (dis)charge durations. Also, note how the proportion of CAPEX associated with the discharging infrastructure for the (τ_{dis} = 32 h, τ_{ch} = 10 h) system increases as its ff_{dis} increases from 1 to 10.

Fig. I.28 shows the maximum grid cost reduction and maximum ROI across the analyzed TEGS configurations with constant-power charging for the NE and TX grids.

Figs. I.27 and I.28 illustrate that grid cost reduction decreases with decreasing TEGS budget as expected since the optimal capacity mix can no longer be installed. Additionally, for the NE grid, shorter duration systems become optimal with decreasing budget to maximize the utilization of the increasing arbitrage opportunities, as discussed in Sections 4.1 and 4.2, while for the TX grid, the optimal configuration generally remains the same irrespective of the available budget probably because even when 100 % of the budget is available, a rather short duration system is optimal.

ROI increases with decreasing TEGS budget. This is due to the inherent nature of electricity dispatch encapsulated in the GenX optimization algorithm wherein the electricity price at an instant corresponds to the cost of generation of the most expensive resource required to fulfill demand at that instant. This means that when optimal capacities are installed, all grid resources will make zero profit. However, when installed capacities decrease, profits will increase since there will be more instances when the most expensive resources are utilized causing the electricity price to be much higher than the generation cost of most resources on the grid. Finally, systems which minimize grid cost generally also offer maximum ROI meaning systems optimal for the grid are also often the most rewarding for the investor.

Thus, the case study reveals that the optimality of a configuration may be subject to the available budget. However, any conflict of interest between minimizing grid cost and maximizing ROI is negligible and a particular TEGS configuration can achieve both objectives.

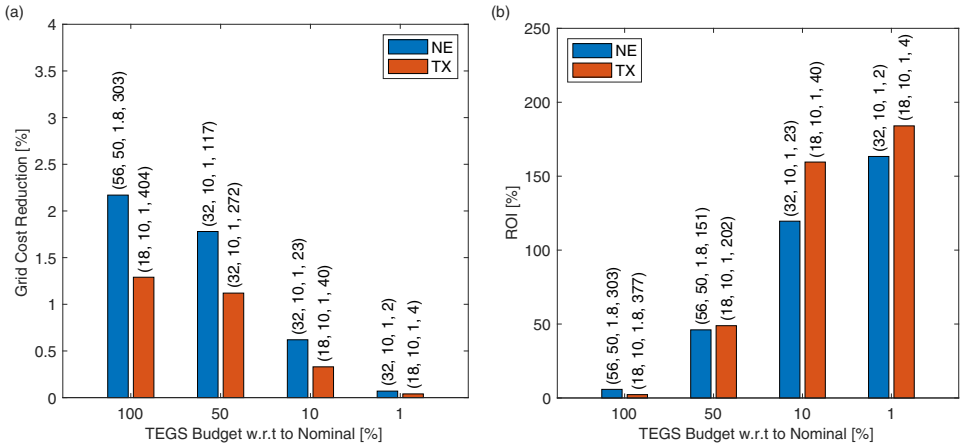

Fig. I.27. (a) Maximum grid cost reduction and (b) maximum ROI across TEGS configurations with constant-power discharging for the NE and TX grids when 100 %, 50 %, 10 % and 1 % of the nominal, unconstrained TEGS budget is available. Only the configuration producing the maximum cost reduction and ROI in each budget scenario has been shown, represented as a (τ_{dis}, τ_{ch}, ff_{ch}, E (MWh)) quadruplet.

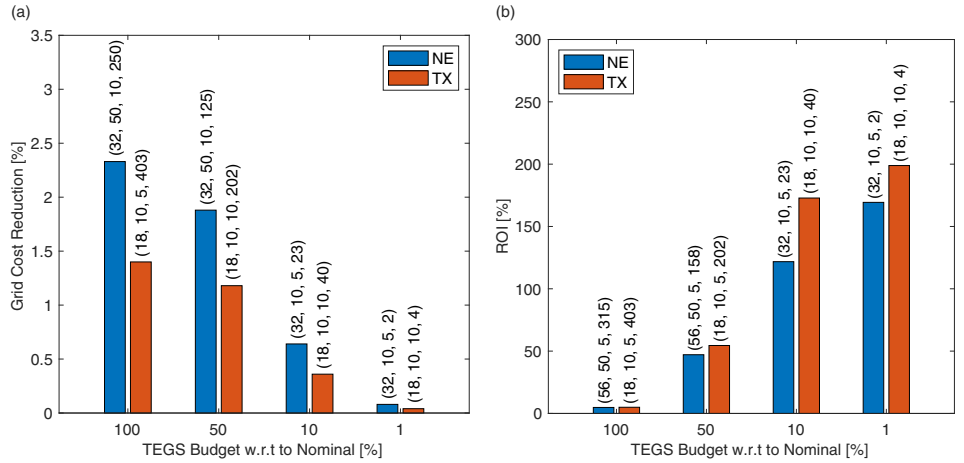

Fig. I.28. (a) Maximum grid cost reduction and (b) maximum ROI across TEGS configurations with constant-power charging for the NE and TX grids when 100 %, 50 %, 10 % and 1 % of the nominal, unconstrained TEGS budget is available. Only the configuration producing the maximum cost reduction and ROI in each budget scenario has been shown, represented as a (τ_{dis}, τ_{ch}, ff_{ch}, E (MWh)) quadruplet.

Data availability

Link to data: https://github.com/AshwinSandeep1/TEGS.

References

[1] IEA. World energy outlook 2020. 2020. https://www.iea.org/reports/world-energy-outlook-2020

[2] Braff WA, Mueller JM, Trancik JE. Value of storage technologies for wind and solar energy. Nat Clim Chang 2016;6(10):964–69.

[3] Apostoleris H, Sgouridis S, Stefancich M, Chiesa M. Utility solar prices will continue to drop all over the world even without subsidies. Nat Energy 2019;4(10):833–34.

[4] Burian O, Dančová P. Compressed air energy storage (Caes) and liquid air energy storage (Laes) technologies—a comparison review of technology possibilities. Processes 2023;11(11):3061. https://doi.org/10.3390/pr11113061

[5] Ziegler MS, Mueller JM, Pereira GD, Song J, Ferrara M, Chiang Y-M, et al. Storage requirements and costs of shaping renewable energy toward grid decarbonization. Joule 2019;3(9):2134–53.

[6] Albertus P, Manser JS, Litzelman S. Long-duration electricity storage applications, economics, and technologies. Joule 2020;4(1):21–32.

[7] Amy C, Seyf HR, Steiner MA, Friedman DJ, Henry A. Thermal energy grid storage using multi-junction photovoltaics. Energy Environ Sci 2019;12(1):334–43.

[8] Kelsall CC, Buznitsky K, Henry A. Technoeconomic analysis of thermal energy grid storage using graphite and tin. arXiv preprint arXiv:2106.07624; 2021.

[9] Verma S, Kelsall C, Buznitsky K, LaPotin A, Sandeep A, Henry A. Designing for effective heat transfer in a solid thermal energy storage system. arXiv preprint arXiv:2402.07764; 2024.

[10] Enescu D, Chicco G, Porumb R, Seritan G. Thermal energy storage for grid applications: current status and emerging trends. Energies 2020;13(2):340. https://doi.org/10.3390/en13020340.

[11] LaPotin A, Schulte KL, Steiner MA, Buznitsky K, Kelsall CC, Friedman DJ, et al. Thermophotovoltaic efficiency of 40%. Nature 2022;604(7905):287–91.

[12] Verma S, Buznitsky K, Henry A. Thermophotovoltaic performance metrics and technoeconomics: efficiency vs. power density. arXiv preprint arXiv:2407.00940; 2024.

[13] Sepulveda NA, Jenkins JD, Edington A, Mallapragada DS, Lester RK. The design space for long-duration energy storage in decarbonized power systems. Nat Energy 2021;6(5):506–16.

[14] Li P, Huang Y, Qi W, Gan J. Capacity co-optimization of thermal and battery energy storage system in multi-energy complementary system. In: 2019 IEEE innovative smart grid technologies - Asia (ISGT Asia); 2019. p. 3815–19. https://doi.org/10.1109/ISGT-Asia.2019.8881407

[15] Denholm P, King JC, Kutcher CF, Wilson PP. Decarbonizing the electric sector: combining renewable and nuclear energy using thermal storage. Energy Policy 2012;44:301–11. https://doi.org/10.1016/j.enpol.2012.01.055 https://www.sciencedirect.com/science/article/pii/S030142151200081X

[16] Li Z, Zhi X, Wu Z, Qian G, Jiang R, Wang B, et al. Role of different energy storage methods in decarbonizing urban distributed energy systems: a case study of thermal and electricity storage. J Energy Storage 2023;73:108931. https://doi.org/10.1016/j.est.2023.108931 https://www.sciencedirect.com/science/article/pii/S2352152X23023290

[17] Amini Toosi H, Lavagna M, Leonforte F, Del Pero C, Aste N. Building decarbonization: assessing the potential of building-integrated photovoltaics and thermal energy storage systems. Energy Rep 2022;8:574–81. https://doi.org/10.1016/j.egyr.2022.10.322 https://www.sciencedirect.com/science/article/pii/S2352484722022570

[18] Eikeland OF, Kelsall CC, Buznitsky K, Verma S, Bianchi FM, Chiesa M, et al. Power availability of pv plus thermal batteries in real-world electric power grids. Appl Energy 2023;348:121572.

[19] Eikeland OF. Enhancing decision-making in the electric power sector with machine learning and optimization, [Ph.D. thesis], The Arctic University of Norway, 2023.

[20] Jenkins JD, Sepulveda NA. Enhanced decision support for a changing electricity landscape: The Genx configurable electricity resource capacity expansion model. 2017.

[21] Roy-Layinde B, Lim J, Arneson C, Forrest SR, Lenert A. High-efficiency air-bridge thermophotovoltaic cells. Joule 2024;8(7):2135–45.

[22] C. Inc. Comsol. Comsol. 2020. http://www.comsol.com/products/multiphysics/

[23] Gurobi Optimization, LLC. Gurobi optimizer reference manual. 2023. https://www.gurobi.com

[24] Wächter A, Biegler LT. On the implementation of an interior-point filter line-search algorithm for large-scale nonlinear programming. Math Program 2006;106(1):25–57.